

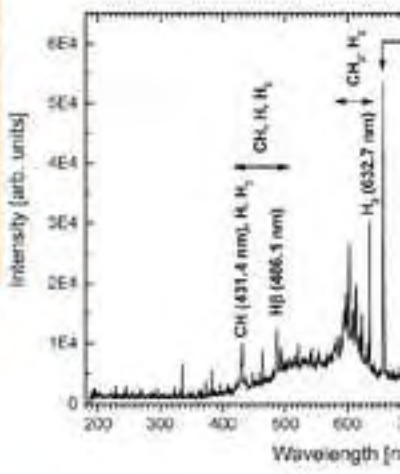
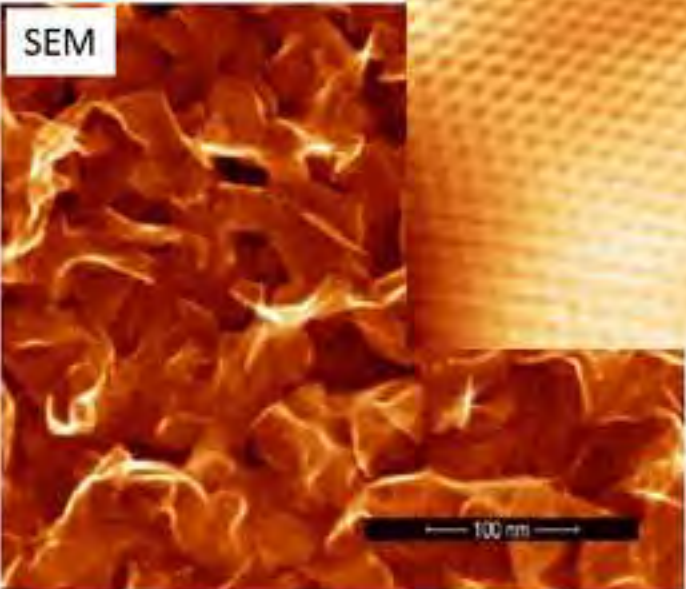
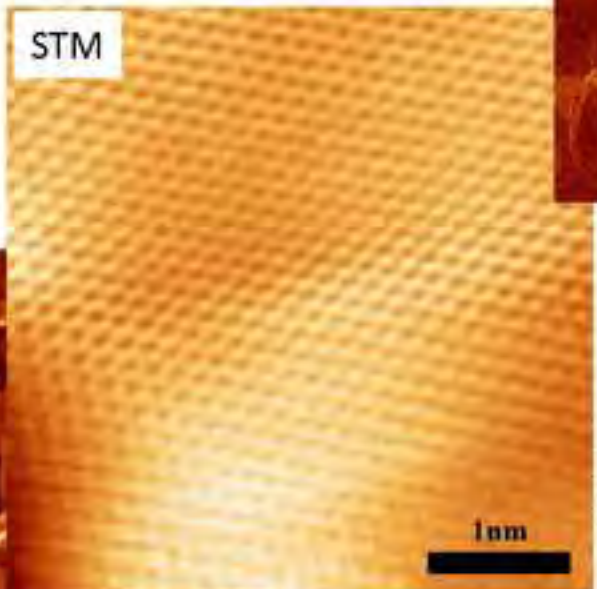
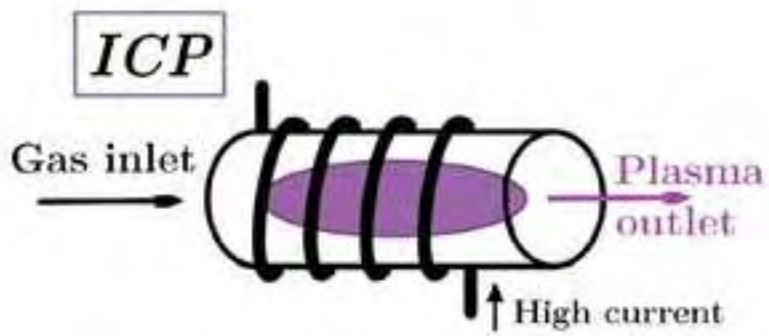
This is the accepted version of the following article:

Cuxart M.G., Šics I., Goñi A.R., Pach E., Sauthier G., Paradinas M., Foerster M., Aballe L., Fernandez H.M., Carlino V., Pellegrin E.. Inductively coupled remote plasma-enhanced chemical vapor deposition (rPE-CVD) as a versatile route for the deposition of graphene micro- and nanostructures. Carbon, (2017). 117. : 331 - .
10.1016/j.carbon.2017.02.067,

which has been published in final form at

<https://dx.doi.org/10.1016/j.carbon.2017.02.067> ©

<https://dx.doi.org/10.1016/j.carbon.2017.02.067>. This manuscript version is made



Inductively Coupled Remote Plasma-Enhanced Chemical Vapor Deposition as a Versatile Route for the Deposition of Graphene **Micro- and** **Nanostructures.**

M. G. Cuxart^{a1}, I. Šics^a, A. R. Goñi^{b,c}, E. Pach^d, G. Sauthier^d, M. Paradinás^d, M. Foerster^a, L. Aballe^a, H. Moreno Fernandez^a, V. Carlino^e, E. Pellegrin^{a,*2}

^a ALBA Synchrotron Light Facility, Carrer de la Llum 2-26, 08290 Cerdanyola del Vallès, Spain.

^b Institut de Ciència de Materials de Barcelona (ICMAB-CSIC), Campus UAB, Bellaterra, Spain.

^c ICREA, Passeig Lluís Companys 23, 08010 Barcelona, Spain.

^d Catalan Institute of Nanoscience and Nanotechnology (ICN2), CSIC and The Barcelona Institute of Science and Technology, Campus UAB, Bellaterra, 08193 Barcelona, Spain

^e ibss Group Inc., Burlingame, CA 94010, USA.

Abstract

Multiple layers of graphene thin films with **micro-crystalline orientation** and vertical graphene nano-sheets were grown on different substrates (i.e., polycrystalline nickel foil, Ni(111), highly oriented pyrolytic graphite) using a single-step process based on low-pressure remote Plasma-Enhanced Chemical Vapor Deposition (rPE-CVD). **In contrast to previous studies, a novel basic approach to this technique including a new *remote* inductively coupled RF plasma source has been used** to (i) minimize the **orientational effect** of the plasma electrical fields **during the catalyst-free growth of graphene nano-sheets**, (ii) warrant for a low graphene defect density via low plasma kinetics, (iii) decouple the dissociation process of the gas from the growth pro-

¹ marc.gonzalez@icn2.cat. Now at the Catalan Institute of Nanoscience and Nanotechnology (ICN2), CSIC and The Barcelona Institute of Science and Technology, Campus UAB, Bellaterra, 08193 Barcelona, Spain

² *Corresponding author. Tel.: +34 93 592 4418. E-mail: epellegrin@cells.es

cess of graphene on the substrate, (iv) tune the feedstock gas chemistry in view of improving the graphene growth, and (v) reduce the growth temperature as compared to conventional chemical vapor deposition (CVD). In order to study the various aspects of the rPE-CVD graphene growth modes and to assess the characteristics of the resulting graphene layers Raman spectroscopy, XPS, SEM, and STM were used. **The results give evidence for the successful performance of this new rPE-CVD plasma deposition source, that can be combined with *in situ* UHV-based processes for the production of, e.g, hybrid metal ferromagnet/graphene systems.**

1. Introduction

The electrical and mechanical properties of graphene, in particular its ballistic transport properties, have opened up exciting possibilities for this material as a replacement for silicon [1, 2]. Graphene has a simple structure, consisting of a honeycomb arrangement of carbon atoms in a monoatomic layer (with a lattice parameter $a_{gr} = 2.46 \text{ \AA}$), and is mechanically and chemically stable. Mechanical exfoliation of highly oriented pyrolytic graphite (*HOPG*) has been the most common method for producing single layers of this material. However, the lateral dimensions of such monolayer samples are typically limited to the micro-
5 scale. Since large area of defect-free graphene films on insulating substrates are required for practical applications, several techniques have been explored such as the reduction of oxidized graphite films, graphitization of SiC wafers under
10 ultra-high vacuum chemical vapor deposition (*CVD*) on transition metals etc.

Recently, several authors [1, 2, 3, 4, 5, 6, 7] have reported new graphene
15 deposition methods using inductively-coupled RF plasma (ICP) as one way to decouple the gas dissociation process from the graphene substrate growth process within the context of Plasma Enhanced Chemical Vapor Deposition (*PE-CVD*). This makes this method more tunable as compared to classical CVD as it allows for an independent control of precursor gas dissociation and growth
20 parameters, which should lead to a better control over the size and shape of

the resulting **carbon** nanostructures. Moreover, using the precursor gas in plasma state involves, by definition, an enhanced density of chemically active carbon radicals, thus enhancing the deposition rate especially in the case of non-equilibrium low-temperature plasma such as the above ICP RF plasma, including a weakly ionized environment with a relatively high electron energy. By using a highly reactive precursor such as a hydrocarbon gas, one can thus decrease the growth/deposition time and/or the substrate temperature. This latter feature opens the graphene deposition process to a wider variety of substrates with low melting points avoiding, e.g., surface roughening as well as the temperature-induced diffusion of carbon atoms into the substrate, resulting in the subsequent carbon surface segregation after sample cooldown. In addition, further intrinsic CVD limitations like, e.g., the single monolayer growth limit of graphene onto Ni(111) can easily be defeated by overcoming the passivation of the graphene monolayer on Ni(111), thus increasing the flexibility of PE-CVD processes further.

Regarding the growth of planar graphene, Boyd et al. [3] have proposed a simple single-step direct PE-CVD deposition method using a quartz tube within an Emerson cavity, encompassing high gas partial pressures of 0.3 *mbar* (i.e., 0.4% CH_4 , 0.4% N_2 , H_2 balance) together with a direct plasma and electric field exposure of the Cu foil, Cu(100), and Cu(111) sample substrates, with the good quality graphene therefore being limited to the substrate side not facing the plasma. Nandamuri et al. [4] were using remote PE-CVD on Ni foil and Ni(111), with an ICP plasma at relatively high partial gas pressures of 0.12 *mbar* (i.e., 23.8% CH_4 , H_2 balance) in a non-UHV compatible quartz tube reactor setup. On a similar technological basis, Zhang et al. [6, 7] were depositing at similar pressures of 0.266 *mbar* (i.e., pure CH_4) on wide range of substrates with rather long deposition times of up to 3 hours for a graphene coverage of 2-3 monolayers resulting into 100 *nm* graphene patches on HOPG and nano-crystalline entities on SiO_2 . Regarding the catalyst-free growth of vertical graphene nano-sheets on Si, Zhu et al. [8] did use PE-CVD with a planar ICP source and a methane (40%)/hydrogen (60%) feedstock gas mixture,

concluding that the correct combination of hydrogen atomic plasma species together with the interaction of the plasma electric field with the growth process results into the growth of vertical graphene nano-sheets.

55 During the last years, CELLS-ALBA [9] together with ibss Group Inc. [10] have acquired a large expertise regarding the generation and handling of *remote* (or downstream) low-pressure ICP RF plasma for the cleaning of carbon contaminations as generated by the interaction of the synchrotron photon beam with residual CO_2 gas molecules etc. at the surface of synchrotron optics, as
60 well as by the electron beam on samples within SEM or TEM setups [11, 12]. An inductively coupled GV10x RF plasma source (ibss Group) has so far been used as a cleaning tool for carbon-contaminated optical surfaces, where the feedstock gas of the plasma consists of a chemically active agent (such as, e.g., oxygen or hydrogen neutral radicals), thus converting the carbon into CO_2 , CO ,
65 or hydrocarbons gas via oxidation or reduction, respectively. In order to preserve the advantages of the above graphene CVD approaches while striving for an improvement of the graphene deposition process towards an enhanced flexibility of the graphene growth modes, a better UHV compatibility of the overall process, and an improved graphene sample quality, we have further developed
70 the rPE-CVD technique using the GV10x plasma source but inverting its operation principle (see Figure 1). From a topological perspective we propose a *remote* ICP plasma generated within a distant/separate plasma tube volume, thus avoiding preferential perpendicular growth directions that electrical fields within a direct plasma deposition process unavoidably incur. Furthermore,
75 the significantly reduced kinetics involved in a *remote* plasma as compared to a *direct* plasma should facilitate a deposition of carbon nano-structures with significantly reduced defect density. The unsurpassed chemical flexibility and tunability of PE-CVD processes supporting the simultaneous reaction of different chemical species makes up a major advantage as compared to traditional
80 CVD processes.[13, 14]. Last but not least, the overall vacuum characteristics of the employed GV10x source result into a deposition process that is compatible with **generic and thus unavoidable** UHV requirements of prior or

subsequent MBE processes, in view of allowing for, e.g., the production of ferromagnet/graphene/ferromagnet hybrid multilayer thin film sample systems.

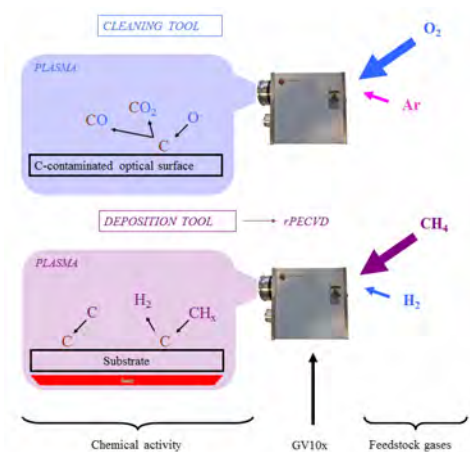


Figure 1: Reversing the GV10x plasma source from a *top-down* plasma cleaning tool to a *bottom-up* deposition tool for remote plasma-enhanced chemical vapor deposition (rPE-CVD).

85 In order to accomplish the purpose of inverting the working principle of the GV10x from a *top-down* cleaning tool to a *bottom-up* deposition tool, several routes for depositing graphene onto different substrates were explored over a wide range of deposition parameters. The substrates studied were Ni foil, HOPG(0001) and Ni(111) (**Note: A complete set of experimental data**
 90 **for the case of the early graphene growth stages on Ni(111) can be found in the Supplementary Content**). The resulting samples were characterized following a systematic approach in order to verify the deposited graphene layer thickness, morphology, defect density etc. Raman spectroscopy (using a laser with 632.8 *nm* wavelength) gives a precise idea of the kind of carbon al-
 95 lotrope and crystalline quality [15]. Scanning Electron Microscopy (SEM) and Scanning Tunnelling Microscopy (STM) yield a direct picture of the sample surface with a nanometric and atomic resolution, respectively. Finally, X-Ray Photoemission Spectroscopy (XPS) gives a detailed chemical analysis of the surface that allows calculating atomic concentrations and thickness in terms of
 100 deposited monolayers. The main point of this characterization procedure is to

cross-check results and to get a more complete picture of the characteristics of the produced rPE-CVD graphene samples, the pertinent growth processes and dynamics as a function of sample substrate and process parameters (e.g., RF power, feedstock gas mixtures, total pressure, substrate temperature etc.).

105 2. Experimental

There are several approaches for creating a plasma using RF electromagnetic (EM) fields. In high pressure plasma, the energy that the electrons have acquired from the EM fields is more likely to be transferred to the heavy ions, because of the higher collision probability. This results into a thermalisation of the whole gas, so that $T_e \simeq T_i = T_{gas}$. Plasma fulfilling this condition are called *thermal plasma* working close to atmospheric pressure. On the other hand, plasmas are termed *non-thermal* when $T_e \gg T_i = T_{gas}$, and they work in lower pressure ranges ($P_{atm} - 10^{-3} \text{ mbar}$). Thermal plasma are usually more powerful, while non-thermal plasma are more selective and are thus typically used for nanotechnology applications. Thus, the GV10x plasma source used in this work produces non-thermal plasma through inductively coupled RF discharges (see below).

There are two well-known methods for the generation of the non-thermal plasma created by RF discharges:

- 120 (i) Capacitively Coupled Plasma (*CCP*): CCP discharges provide the EM field to the gas flow by means of electrodes located either outside or inside of the plasma chamber (see Figure 2). These discharges primarily stimulate a DC or AC electric field in order to facilitate plasma ignition. High AC or DC electric fields are needed for this purpose.
- 125 (ii) Inductively Coupled Plasma (*ICP*): An in-air coil surrounding a ceramic tube inside which the EM fields are induced into the gas flow (see Figure 2). A high RF electric current passes through the coil which induces a high frequency magnetic field along the tube axis. This AC magnetic field induces a high frequency vortex electric field, concentric with the

130 elements of the coil and providing the plasma breakdown and sustaining
the plasma. Non-thermal ICP plasma discharges work at low pressures
(i.e., 10^{-1} to 10^{-3} mbar in our setup), so that the ratio between electric
field and pressure (E/p) is sufficient for ionization. The coupling between
plasma and the coil can be seen as a voltage decreasing transformer, where
135 the coil works as the primary windings and the plasma as the secondary
windings. ICP discharges are operated at high currents, high electron
concentration, and high electrical conductivity.

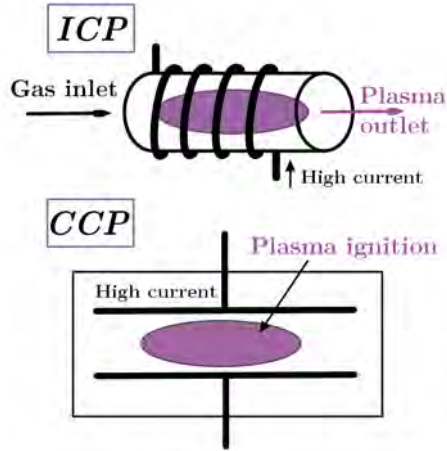


Figure 2: Schematic of the Capacitively Coupled Plasma (CCP) and Inductively Coupled Plasma (ICP) sources.

From the perspective of thin film deposition, the CCP setup includes the
installation of the sample substrate onto one of the capacitor antenna plates
140 (i.e., either connected to the RF source or to ground), thus exposing the sample
directly to the plasma and the associated electric fields together with high-
energy ions and electrons. While this may be desirable for ion-assisted plasma
processes, the growth of graphene thin films with low defect densities will **un-**
avoidably suffer from this [3]. In addition, sputtering products from the an-
145 tenna material or from other chamber parts (especially from the build-up of a
DC bias on floating/insulating parts inside the plasma chamber) may possibly
lead to a corresponding contamination of the thin film and/or the substrate.

On the other hand, *Remote* ICP plasma sources offer the advantage of not exposing the RF coil or antenna material to the plasma (i.e., avoiding a source of plasma and/or thin film contaminations). **In addition**, the inherent geometrical separation of the plasma generation volume from the thin film deposition chamber volume **keeps** the latter free of the EM fields as generated by the upstream RF coil. **Thus, the** overall topology warrants for the low kinetic energies of ions and electrons within the downstream deposition chamber.

Last but no least, it should be pointed out that the high currents and high electron densities as generated in an ICP plasma sources as compared to CCP setups is beneficiary for the efficient production of atomic hydrogen,[13] thus facilitating the defect-free growth of graphene nano-structures at lower hydrogen gas concentrations. This will become apparent from the low hydrogen feedstock gas concentrations used in this study as compared to, e.g., the results from other **PE-CVD graphene deposition** studies mentioned above.

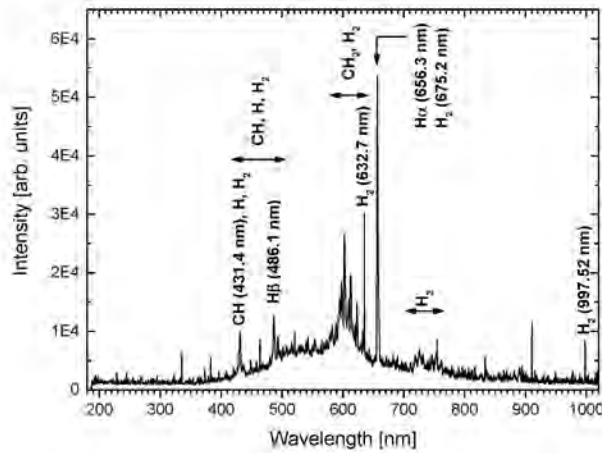
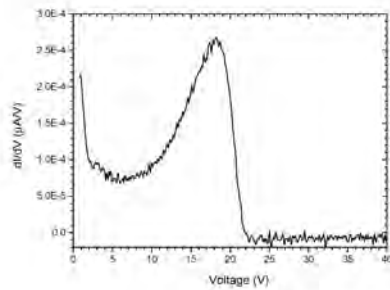


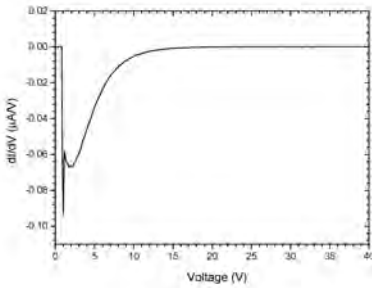
Figure 3: Optical emission spectrum (OES) from the CH_4/H_2 80%/20% feedstock gas plasma used for the growth of the Ni foil sample 3.

Figure 3 shows a typical optical emission spectrum (OES) from a CH_4/H_2 feedstock gas plasma. From this, the atomic type, charge, as well as the precise

165 mixing ratio of the chemically active species within the plasma can be determined, thereby enabling a correlation between the plasma properties and the characteristics of the resulting thin film samples. The evaluation performed using commercial software [16] based on tabulated standard emission spectra.[17] The plasma parameters for this OES were those used for the rPE-CVD growth of graphene of the Ni foil sample **3** (see Table 1).



(a) Ion energy distribution function (IEDF) for Ar cations.



(b) Electron energy distribution function (EEDF).

Figure 4: Typical dI/dV curves based on I-V Faraday cup data taken from a pure Ar feedstock gas plasma (70 W RF power, 0.005 mbar Ar feedstock gas pressure) yielding the Ar cation and electron energy distribution functions at 800 mm from the plasma source.

170 As a further example for the characteristics of the downstream (or afterglow) plasma as generated by the GV10x plasma source during the rPE-CVD deposition process, Figure 4a shows typical dI/dV curves as obtained from Fara-

day cup measurements from a pure Ar plasma (70 W RF power, 0.005 mbar Ar feedstock gas pressure). As the dI/dV curve in Fig. 4a represents the ion energy distribution function (IEDF) for Ar cations, their distinctly low kinetic energies with an average kinetic energy of 13.3 eV could be determined. On the other hand, the electron energy distribution function (EEDF) in Fig. 4b results in an average electron kinetic energy of 4.1 eV. In analogy to these data from a pure Ar plasma, we tentatively expect correspondingly low-energy IEDF and EEDF also for the case of a CH_4/H_2 80%/20 % feedstock gas plasma. As will be shown later on, this warrants for the growth of graphene materials with low defect densities for rPE-CVD deposition in contrast to standard PE-CVD processes based on *direct* plasma deposition in conjunction with high electric fields and correspondingly high kinetic energies of the charged species within the plasma.

In the next section, we will show how the above technical aspects of an ICP plasma source within the context of a **UHV-based rPE-CVD sample preparation chamber setup** combine into the efficient deposition of high-quality **micro-crystalline graphene layers and vertical** graphene nano-sheets.

3. Results and Discussion

The main techniques used to characterize our samples were Raman spectroscopy and SEM. Room temperature STM measurements were carried out for selected samples in order to assess the quality of the graphene foils at the atomic level (i.e., the density of defects as vacancies, antisites, dislocations, boundaries, etc.). Raman spectra of our samples typically show the three characteristic peaks denoted D (1345 cm^{-1}), G (1583 cm^{-1}) and $2D$ ($\sim 2690\text{ cm}^{-1}$) [18, 15, 19].

According to common knowledge, the following features turn out to be the best fingerprints for graphene (see **Fig. 1 in the Supplementary Content document**):

- (i) The position of the G peak should be up-shifted by $3-5\text{ cm}^{-1}$ with respect to that of bulk graphite.[20]
- (ii) The 2D peak in bulk HOPG consists of two components, with roughly 1/4 ($2D_1$) and 1/2 ($2D_2$) the height of the G peak, whereas a single and sharper 2D peak should be observed in graphene, down-shifted by $\sim 35\text{ cm}^{-1}$. [18]
- (iii) The ratio between 2D and G peak exhibits a drastic change in favour of the 2D. [15, 18, 21]

The widths of the individual peaks are crucial in order to estimate the quality of the graphitic sample, and thus to evaluate the contribution of the disordered phase (i.e., amorphous carbon) among the pure sp^2 phase [15]. Samples with a high degree of amorphous carbon (i.e., a mixture with various amounts of sp^2 and sp^3 bonds) show wider D and G peaks, sometimes described as a single down-shifted broad G band centred at $\sim 1500\text{ cm}^{-1}$.

Table 1 gives an overview of the samples as well as the preparation parameters used for the rPE-CVD deposition processes in the present study.

3.1. Growth of nano-crystalline graphene sheets on polycrystalline Ni foil

Polycrystalline Ni foils ($7.5\text{ }\mu\text{m}$ thickness) were pre-cleaned by ultrasound in acetone and ethanol before introduction into the vacuum system in order to remove adhered particles on the surface. Once introduced into the chamber, the Ni foils were degassed at 500°C for at least $2h$, so that physisorbed molecules and weakly chemisorbed molecules were removed. Substrates were warmed up to different temperatures (between 625 and $725\text{ }^\circ\text{C}$) and exposed to $CH_4(80\%)/H_2(20\%)$ plasma at 0.1 or 0.01 mbar , for different time periods (1 , 3 and 5 min) and different RF powers (100 and 200 W) [4]. Please note the short deposition times as compared to some CVD processes.

It is well-known that atomic hydrogen plays an important role in carbon thin film growth by removing amorphous and sp^3 hybridized carbon faster than sp^2 hybridized carbon [8]. Hence, the amount of hydrogen radicals (i.e., as compared to pure CH_4 feedstock gas) was increased by introducing additional H_2 gas into the feedstock gas mixture.

Table 1: Summary of experimental conditions for each sample reported in this work (**Note: Data corresponding to graphene samples synthesized on Ni(111) are shown in the Supplementary Content**).

Sample no., substrate, and result	Feedstock gases	RF Power [W]	Pressure [mbar]	Temp. [°C]	Exp. Time [min]
<i>1</i> Ni foil, partial coating	CH ₄ /H ₂	207	1.0 · 10 ⁻¹	715	1
<i>2</i> Ni foil, shrink wrap	CH ₄ /H ₂	191	1.0 · 10 ⁻¹	725	3
<i>3</i> Ni foil, cont. shrink wrap	CH ₄ /H ₂	207	1.0 · 10 ⁻¹	725	5
<i>4</i> Ni foil, thick disordered	CH ₄ /H ₂	201	1.0 · 10 ⁻²	720	5
<i>5</i> Ni foil, nucleation	CH ₄ /H ₂	99	1.0 · 10 ⁻¹	625	5
<i>6</i> Ni foil, granular growth	CH ₄	207	1.0 · 10 ⁻¹	740	5
<i>1</i> Ni(111), partial coating	CH ₄ /H ₂	180	1.0 · 10 ⁻¹	725	5
<i>2</i> Ni(111), nucleation	CH ₄ /H ₂	189	1.0 · 10 ⁻¹	625	5
<i>1</i> HOPG(0001), 2D growth	CH ₄ /H ₂	99	2.0 · 10 ⁻¹	600	180
<i>2</i> HOPG(0001), nano-sheets	CH ₄ /H ₂	99	1.0 · 10 ⁻¹	600	30

All the typical graphene features in the Raman spectra described above can be observed with different weights for each individual sample as shown in Figure 5 and analyzed in Table 2. Sample *1* presents a Raman spectrum with a very low 2D/G ratio and a low G/D ratio (see Table 2), which suggests that carbon has been deposited in a very disordered manner, leading to a large number of defects such as patch edges together with low number of graphene monolayers. **This is corroborated by the SEM images in Figure 6a, that show inhomogeneously as well as homogeneously coated areas, where we tentatively ascribe the bright spotted areas in the former to domains with an enhanced defect concentration including a partial coating, with both phenomena contributing to the D peak. As can be seen from the PEEM/LEEM results in the Supplementary Content, these micron-size bright/spotted domains during the further growth process evolve into carbon-coated non-crystalline domains, in contrast**

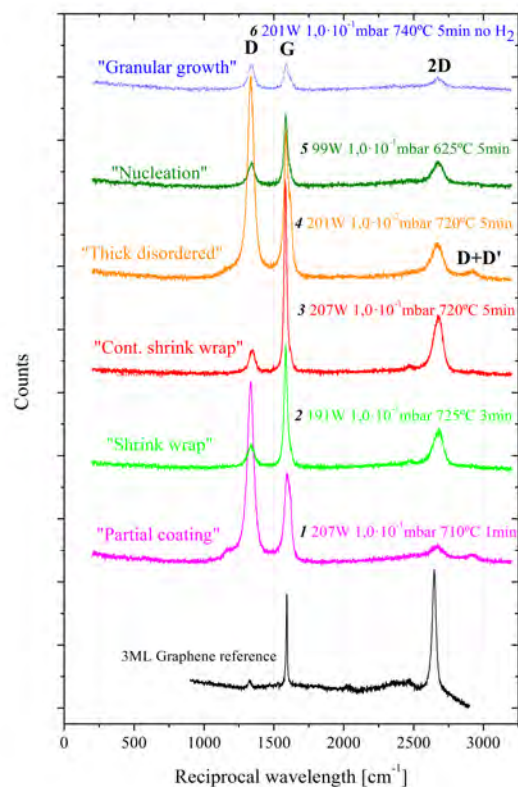


Figure 5: Raman spectra of PECVD graphene samples **1** to **6** grown on Ni foil substrates, together with a 3 ML-graphene reference sample.

to the dark graphene domains exhibiting crystalline characteristics.

These darker domains in Figure 6a yield **a distinct** homogeneous graphene coverage (see also **Figure 6b for more detail**) in form of a wrinkled semi-transparent foil. As in the case of CVD graphene on cold-rolled copper foil [22], where the micro-crystalline grains within the Cu foil surface are known to predominantly reorient with a (100) surface termination at the elevated temperatures used during CVD growth of graphene, we conclude that areas with different amounts of graphene coverage - coinciding with the domains of the Ni micro-crystals - depend on the orientation of the micro-crystals within the Ni foil surface, thus influencing the graphene growth rate. Everything considered,

Table 2: Qualitative analysis of the graphene features measured in each sample on Ni foil. (a), (b) and (c) refer to the three Raman fingerprints of graphene: Shift of G peak, width of the 2D peak, and ratio between 2D and G peaks. The last column with the ratio between the G and the D peaks intensities gives a relative measure of the amount of defects within the graphene layers. The D' peak were taken into account for the intensity evaluation of the G peak.

Sample no., substrate, and result	(a) $pos_G(\text{meas.})$ - $pos_G(\text{HOPG})$ [cm^{-1}]	(b) I_{2D}/Width_{2D} [cm]	(c) I_{2D}/I_G	(d) I_G/I_D
(1) Ni foil, partial coating	10.3	0.23	0.18	0.32
(2) Ni foil, shrink wrap	2.9	1.32	0.86	2.27
(3) Ni foil, cont. shrink wrap	1.2	2.51	0.78	3.88
(4) Ni foil, thick disordered	5.2	0.92	0.46	0.44
(5) Ni foil, nucleation	3.2	0.75	0.81	1.53
(6) Ni foil, granular growth	8.8	1.28	0.58	0.81

these results speak in favour of increasing the (low) deposition time (1 *min*) as used for sample **1**. The area with a low graphene coverage in the SEM image for sample **1** (see Fig. 6a), are reminiscent of the early rPE-CVD growth stage of graphene on Ni(111) **discussed in the Supplementary Content (see Fig. 3c in this document)**. There, we could observe an evolution from "spider"-shaped seed patches at the edges of the Ni(111) terraces via higher deposition temperature into the larger graphene patches also seen for the Ni foil sample **1** in Fig. 6a.

We thus speculate that the low/slow graphene growth areas do correspond to Ni micro-crystals with (111) surface orientation, while other areas including larger growth rates do represent other Ni surface orientations. An in-depth micro-LEED or low-energy electron microscopy (LEEM) analysis would be needed in order to prove this point.

Samples **2**, **3**, and **5** show similar Raman spectra, but now with strongly reduced defect concentrations (see Figure 5). Also, samples **2** and **3** exhibit higher

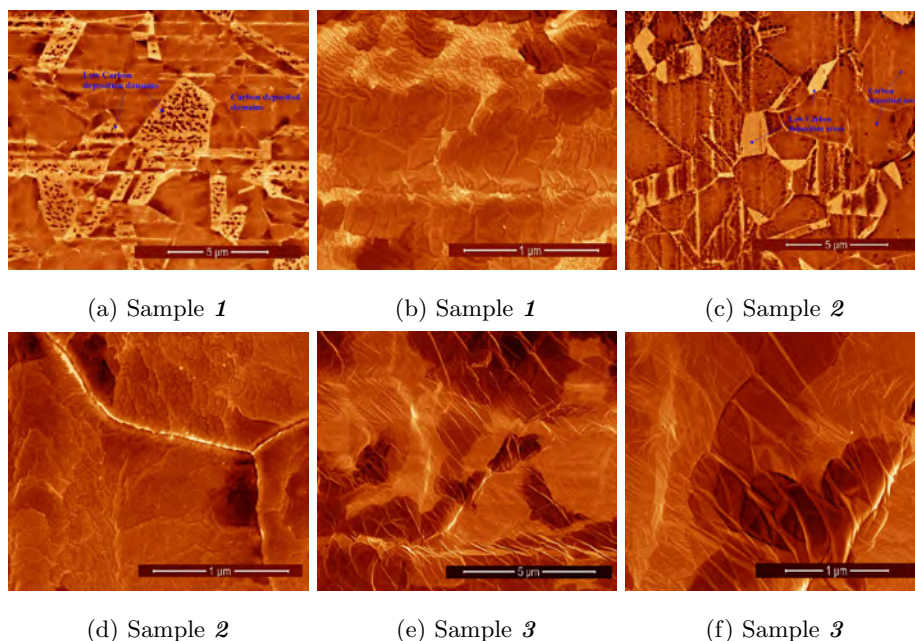


Figure 6: SEM images for sample **1**; Sample **2**; Sample **3** "Shrink wrap". All of them grown on polycrystalline Ni foil.

absolute intensities as well as a sharper 2D peak than in sample **5** (as seen in the I_{2D}/Width_{2D} ratio in Table 2), which can be explained by the higher synthesis temperature of the former two samples ($\sim 725^\circ\text{C}$ against 625°C). This is confirmed in the SEM images: Sample **2** (3 min) shows a more extensive and more homogeneous graphene coverage than sample **1** (1 min deposition time; see Figs. 6c and 6d). Sample **3** (3 min) shows a thicker and very homogeneous graphene coverage (referred to as "shrink wrap") and appears to be in an advanced stage of growth. In contrast to this, sample **5** only exhibits a partial "shrink wrap" appearance (Figure 7c and 7d), and is still mostly transparent with respect to the micro-crystalline domains of the nickel substrate (see the SEM images for the clean nickel reference substrate in the Supplementary Content). The nucleation stage of the graphene growth in this sample **5** can be explained by both the lower substrate temperature and the lower plasma RF power applied during the growth process. We also note that sample **3** appears to be the only sam-

285 ple where the growth of the graphene layer extends seamlessly across the grain
boundaries within the Ni foil surface, thus apparently overcoming the differences
between the Ni micro-crystals during the initial rPE-CVD growth process. **The**
microstructural PEEM/LEEM analysis of sample 3 presented in the
Supplementary Content gives evidence for the micron-size lateral ex-
290 **tension of the crystalline graphene domains on the Ni foil surface, in**
close correspondence to the size of the micro-crystalline Ni surface
domains.

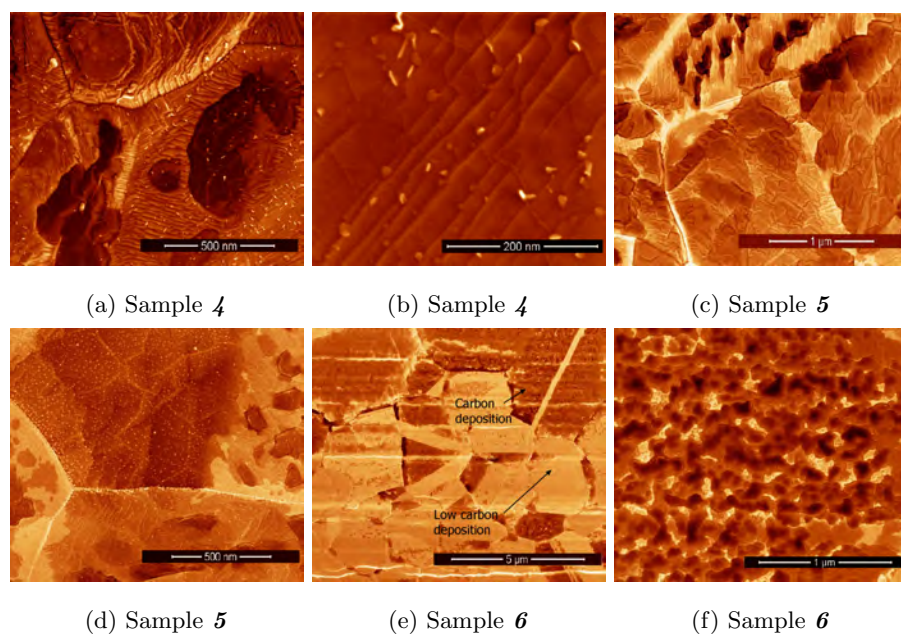


Figure 7: SEM images for sample 4 "Thick disordered layers"; Sample 5 "Nucleation"; Sample 6 "Granular growth". All of them grown on polycrystalline Ni foil.

Samples 1 and 4 present high D peaks: Too short deposition times (1 min
for sample 1) or low deposition pressures (0.01 mbar for sample 4) turned out
295 to be non-optimum. A lower plasma feedstock gas pressure implies a larger mean
free path length for the chemically active carbon and hydrogen radicals within
the plasma (as obvious from a brighter downstream plasma inside the deposi-
tion chamber), thus inducing an accelerated, rather three-dimensional graphene

”step flow” growth process resulting into a **thick disordered** graphene depo-
sition. **The consequences resulting from this accelerated 3D growth**
300 **mode can be observed from the resulting rather complex and thick**
disordered stepped carbon terrace structures in Figure 7a and 7b,
which include a large density of boundaries at the step edges, the
deposition of scattered grains of about 20 nm length (see Figure 7b),
305 **and a larger contribution of an amorphous carbon phase that broad-**
ens the Raman peaks (see Figure 5). Since the characteristic diamond
peak (1332 cm^{-1} [23]) is located very close to the D peak, we speculate that
the growth of a sp^3 phase in sample 4 may also induce the broadening of the D
peak as observed in samples 1 and 4 as compared to, e.g., sample 3. **With the**
310 **overall surface morphology of sample 4 appearing to be rather com-**
plex, the internal chemical/structural aspects of the above stepped
terraces could not be investigated with the experimental tools being
at hand and are presently not clear.

X-ray photoelectron spectroscopy (XPS) measurements were carried out us-
315 ing a monochromatized Al K_α X-Ray source. In addition to the SEM images
giving evidence for the different 2D versus 3D growth modes induced by the
lower deposition pressure when going from sample 3 to 4, the XPS survey spec-
tra shown in Fig. 8 further corroborate the larger graphene layer thickness for
the latter via the larger C1s/Ni2p XPS line ratio, which is also reflected by
320 its smaller I_{2D}/I_G ratio. Thus, we conclude that a factor of ten in the plasma
deposition pressure (while keeping all other parameters constant) results in a
significant changeover in the growth characteristics as well as the underlying
graphene growth mechanisms, indicating a high dynamical criticality of the
graphene growth via rPE-CVD.

325 As sample 3 exhibited the lowest defect concentration in the Raman spectra
(see Figure 5) and the most promising SEM pictures in terms of a complete
and homogeneous substrate coverage (see Figures 6e and 6f), an estimation of
the number of nanocrystalline graphene layers was carried out using the above
XPS data together with the SESSA software (Simulation of Electron Spectra

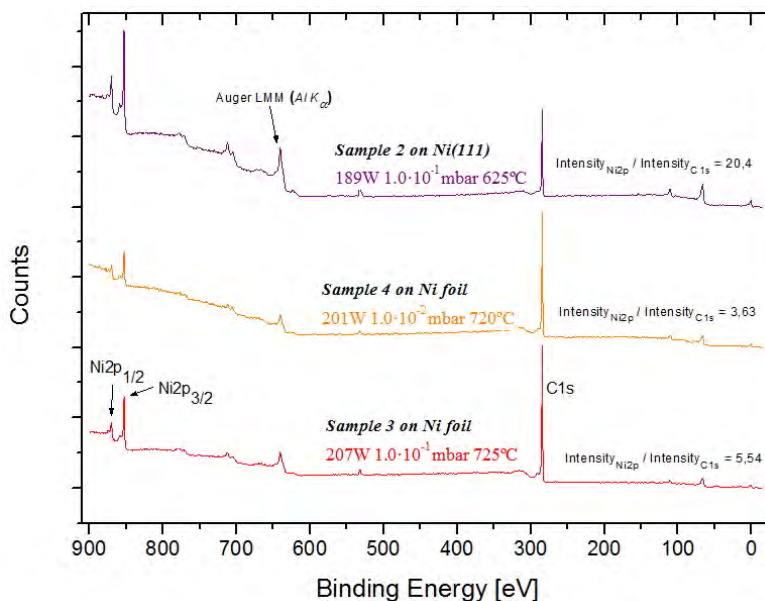


Figure 8: XPS survey spectra of graphene on nickel foil sample **3** (bottom) and **4** (middle), together with the XPS survey spectrum of graphene on Ni(111) sample **2** shown in the Supplementary Content (top).

330 for Surface Analysis [24]). Simulations were based on a simple model of an infinitely thick nickel substrate covered by a thin carbon layer. XPS spectra were simulated for several carbon thicknesses of 3.35 Å (1 monolayer (1GL)), 6.70 Å (2GL), 10.05 Å (3GL), 13.40 Å (4GL), 16.75 Å (5GL), 20.10 Å (6GL) and 23.45 Å (7GL) (one carbon/graphene layer (GL) corresponding to 3.35 Å
 335 thickness [25]) and compared with the measured XPS overview spectrum.

As can be observed in Figure 9, the C1s and Ni2p peak intensities and peak ratios of the 6 ML simulation and the measured XPS overview spectrum match each other quite accurately ($\eta_{Ni2p_{1/2}} = 29.1\%$, $\eta_{Ni2p_{3/2}} = 1.1\%$ and $\eta_{C1s} = 4.2\%$). η_{peak} values are the relative errors between the simulated and
 340 measured intensity for each peak.

Based on the observation that sample **3** exhibits a 6 ML graphene coverage while still maintaining the graphene layer quality, we conclude that the rPE-CVD deposition technique obviously easily overrides the intrinsic graphene

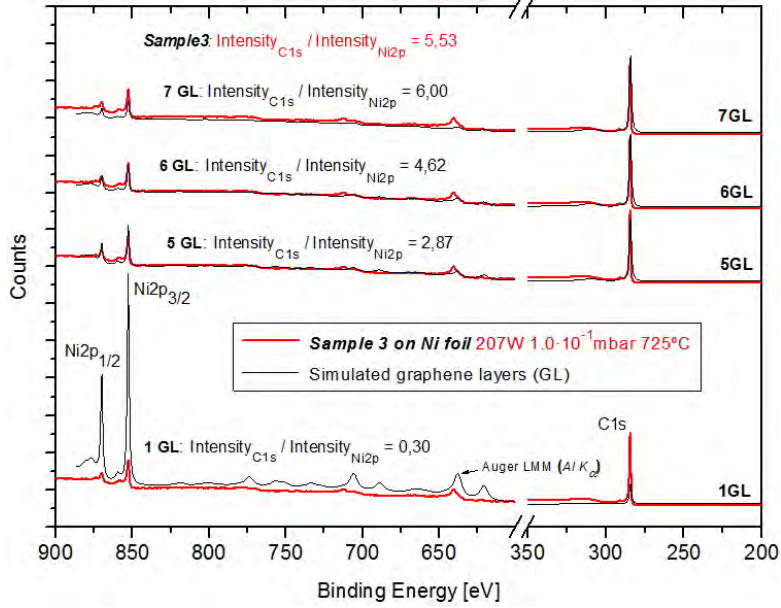
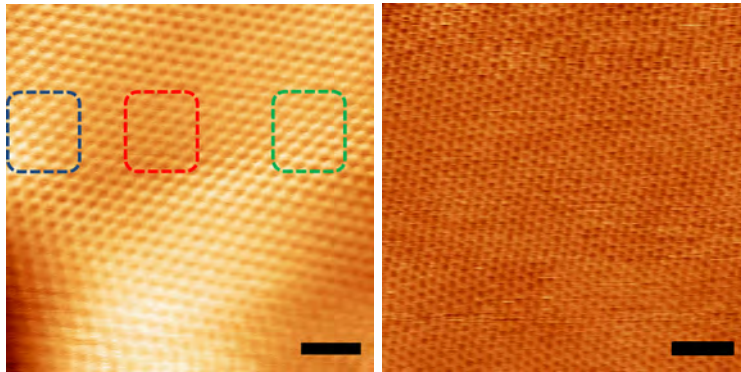


Figure 9: XPS spectrum of graphene on nickel foil **3** (red solid line), together with the simulated XPS spectra calculated with SESSA ranging from one to seven carbon monolayers on a thick nickel substrate (black solid lines).

monolayer limitation on, e.g., Ni(111) surfaces by overcoming the passivating ef-
 345 fect of a graphene monolayer on Ni surfaces (as can be expected from a PE-CVD process).

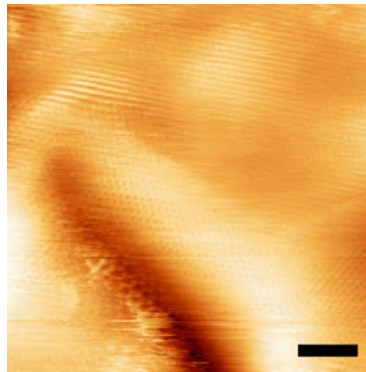
Atomically-resolved STM images corresponding to sample **2** shown in Fig. 10 were measured on different macroscopic regions that represent distinct topo-
 350 graphic features: (i) a flat area where the characteristic honeycomb lattice of the graphitic materials is observed (Fig. 10b); (ii) a wavy area close to a defect of the polycrystalline Ni substrate (Figs. 10a and 10c, where regions exhibiting different periodic structures: honeycomb, hexagonal and stripped patterns (red, blue, and green dashed squares, respectively), that suggest the presence of regions with different graphene layer stacking sequences [26, 27]. In Fig.10c, local in-plane compressions/expansions of the graphene network are responsible of the smooth transitions through substrate domains, thus quenching the Nickel boundary defects, and maintaining the film quality (see Fig. 10c). More-
 355

over, monocrystalline flakes of at least $100 \times 100 \text{ nm}^2$, exhibiting a defect-free
graphene lattice were measured by STM, which is consistent with the low de-
fect peak measured for this sample by Raman (Figure 5). The characteristics
360 of the film as shown in these STM images for sample 2 should also be typical
for sample 3, due to the similar non-linear growth parameters (i.e., RF power
and pressure) and SEM appearances.



(a) Scale bar 1 nm

(b) Scale bar 1.4 nm



(c) Scale bar 2 nm

Figure 10: High-resolution STM images of sample 2 measured at room temperature.

Topographic images of sample 2 were measured at room temperature using
a variable-temperature STM (SPECS, STM Aarhus 150) and processed using a
365 freeware software (WSxM 5.0 develop 6.5) [28].

As another important parameter regarding the growth of graphene thin films,

we have studied the effect of H_2 when used as an additional plasma feedstock gas by comparing the Raman spectra of two samples grown under the otherwise identical conditions (i.e., samples **3** and **6**), but without H_2 in the latter case (see sample **6**, Figure 5). The G/D peak ratio turns out to be much lower, and the 2D peak appears to be broader for sample **6** (see I_{2D}/Width_{2D} ratio in Table 2). The SEM images for sample **6** corroborate this, since apart from the graphitic growth mode, there is a three-dimensional growth that comes together with a granular texture (Figure 7e, zoomed in Figure 7f). Hence, this confirms that the presence of H_2 as an addition to the feedstock gas in the plasma favors the growth rate of sp^2 phases as compared to other phases like, e.g., sp^3 and/or (mixed) amorphous phases. According to our previous experience using the GV10x as a plasma source to clean carbon contaminations, this result does not come as a surprise. The cleaning rates of different carbon depositions measured in our experiments using H_2/Ar plasma revealed that sp^3 carbon cleans faster (1.22Å/ min) than amorphous carbon (0.59Å/ min).[12] Since amorphous carbon mostly consists of a mix of sp^2 and sp^3 , one can conclude that the presence of sp^2 slows down the reaction during the cleaning process or, in other words, sp^3 -bonded or amorphous carbon is more likely to be converted into hydrocarbons by means of hydrogen radicals during the H_2/Ar plasma cleaning while sp^2 -bonded carbon is preserved.

An analysis of the $C1s$ XPS spectrum of sample **3** (see Figure 11) reveals the relative concentration of carbon species within the total carbon content (see table insert in Figure 11). As expected, graphitic carbon (sp^2 at 284.5 eV binding energy (BE), forming the 2-dimensional hexagonal lattice) is the most dominant contribution (67.1%), plus some diamond-like carbon (sp^3 at 285.2 eV BE, forming a diamond structural phase, 12.6%), some contribution from oxidized carbon (C-O-C at 285.8 eV BE, 14.5%), and the $\pi-\pi^*$ shake-up satellite (295.5 eV BE, 5.8%). The C-O-C contribution in the $C1s$ XPS line as well as the oxygen content in $O1s$ line in the XPS overview spectrum may be explained by the fact that samples have been exposed to the atmospheric air after the graphene growth process when being transferred to the XPS setup.

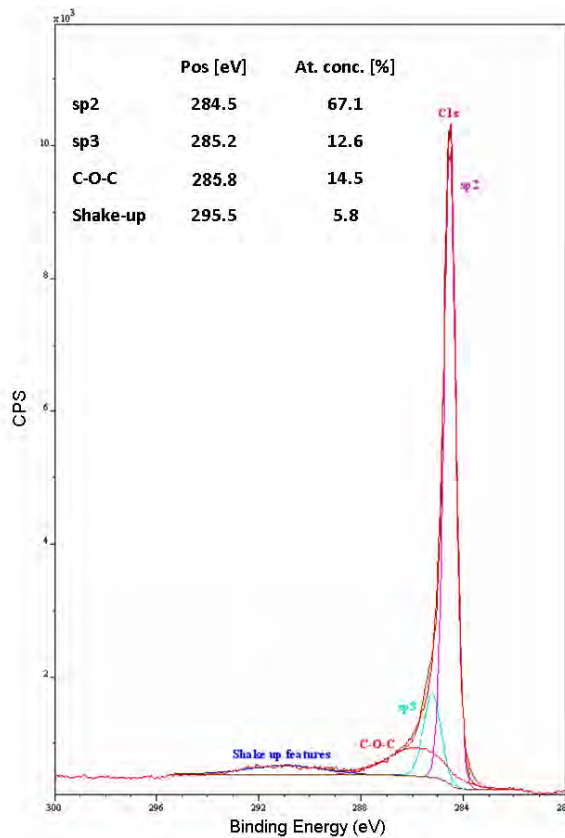


Figure 11: XPS C1s line of the graphene on Ni foil sample **3**, and fitting of its different components (sp^2 , sp^3 , C-O-C and *shake up features*). Table insert: Measured positions of the XPS lines corresponding to the different components in sample **3**, and their relative atomic concentration.

3.2. Catalyst- and field-free growth of vertical graphene sheets on HOPG(0001)

400 We now discuss the rPE-CVD graphene samples **1** and **2** grown onto (0001)-oriented HOPG graphite (see Table 1 for deposition parameters).

A clean HOPG(0001) surface layer was generated by Scotch tape cleaving and subsequently loaded into the UHV chamber where it underwent a degassing process at 400°C for at least $2h$. HOPG(0001) substrates were warmed up to
 405 600°C and exposed to CH_4/H_2 plasma at 0.2 mbar , for 30 and 180 *min*, with a RF power of 100 W).

Both samples show a significantly different behaviour in the Raman spectra (see Fig. 12). Sample **2** closely resembles the Raman spectrum of a clean HOPG(0001) substrate (see the Supplementary Content), which gives evidence that there has not been a significant carbon deposition. On the other hand, the 2D peak in sample **1** tends towards the characteristic shape of graphene already observed for the case of the nickel foil substrates: Peak $2D_1$ increasing at the expense of $2D_2$, the G peak slightly shifted upward (1586 cm^{-1}), together with an extremely large defect peak ($I_G/I_D = 0.26$) as compared to all previously discussed samples. Due to the large D peak in sample **2**, the so-called D' and D+D' peaks also show up, where the D' peak (1620 cm^{-1}) corresponds to a local vibrational mode induced by the high amount of impurities. The latter can interact with the extended phonon modes of graphene, resulting in the splitting of the G peak. [15]

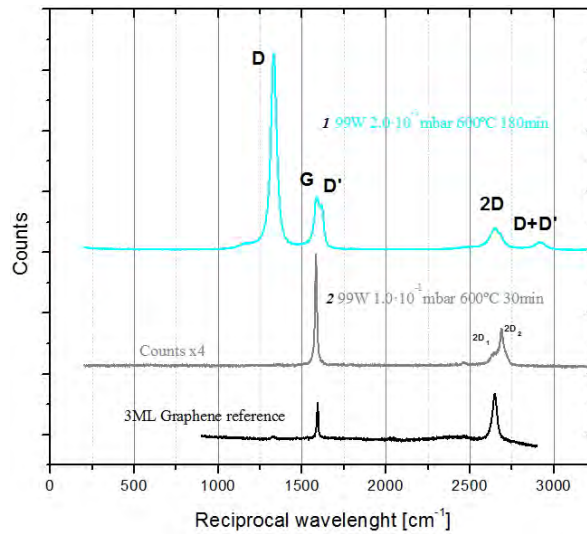


Figure 12: Raman spectra of the collection of rPE-CVD graphene nano-sheet samples **1** and **2** grown on HOPG(0001) (light blue and grey solid line, respectively), together with a 3ML graphene reference sample (black solid line).

In Fig. 13, we show the SEM images of HOPG(0001) samples **1** and **2** as well as the SEM image corresponding to the cleaved pristine HOPG surface. While

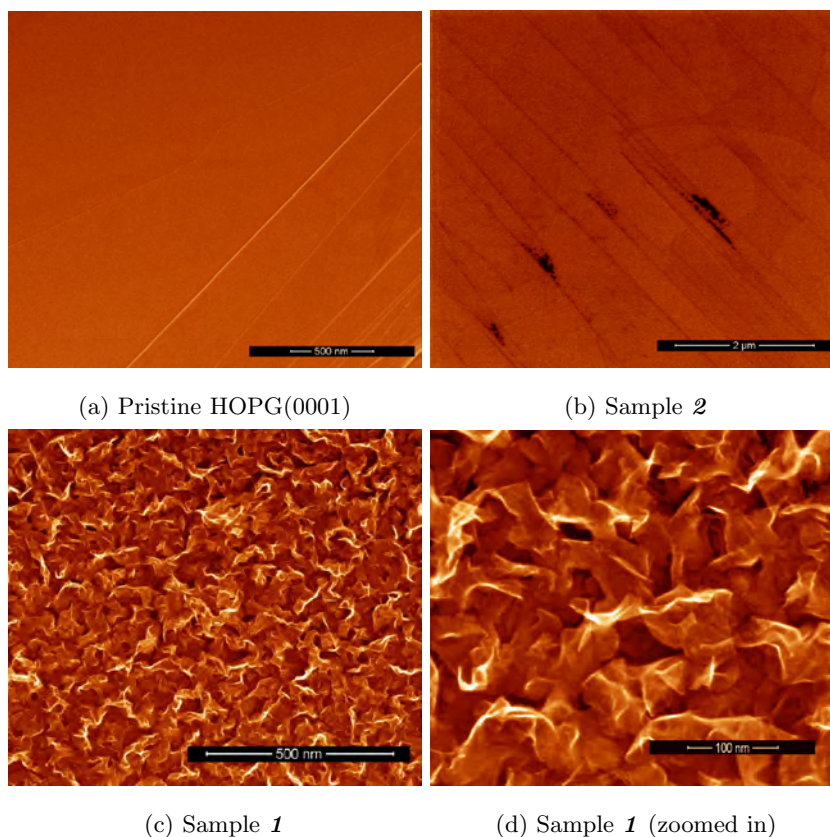


Figure 13: SEM images for freshly cleaved HOPG(0001), samples *1* and *2*, both grown on HOPG(0001).

the pristine HOPG exhibits the typical remarkably flat, clean, and structureless (excepting a few parallel lines due to step edges) planar appearance, the image of sample *2* gives some additional large features on a several micrometer size scale (see Fig. 13b), which we interpret as large-size two-dimensional graphene layers epitaxially grown onto the pre-existing HOPG(0001) surface. Taking into account the rather long deposition time of 30 min. (e.g., as compared to typical Ni deposition times) the large size of the observed additional graphene features does not come as a surprise. The SEM image for sample *1* (see Figs. 13c and 13d) is consistent with the Raman data, as its "vertical nano-sheet" appearance exhibits a considerable amount of sheet edges that largely contribute to the D,

D', and D+D' peaks. From these SEM images, we estimate the thickness of the graphene nano-sheets to be less than 10 graphene monolayers.

As the growth of graphene on HOPG(0001) was expected to synthesize planar homo-epitaxial (or at least epitaxial) graphene due to the inherently perfect
435 lattice matching between the HOPG(0001) and the graphene lattice parameters as can be seen for the case of sample **2**, the above result for sample **1** is surprising. Instead, after a deposition time of 180 min., graphene nano-sheets did grow *vertically* with respect to the HOPG(0001) surface with random in-plane
440 orientation (see Fig. 13d, sample **1**), indicating a switch-over of the graphene growth mode between these two samples from in-plane to vertical (see below).

Sample **1** shows a large amount of graphene nano-sheets (Figure 13c) as well as a high defect concentration in peak D of the Raman spectrum (Figure 12). Meanwhile, in the lower growth limit (30 *min* deposition time), the
445 Raman spectrum of sample **2** (see Figure 12) gives evidence for a graphene deposition that is structurally identical to the HOPG(0001) substrate, and thus indistinguishable from the Raman spectrum of pristine HOPG (see Fig. ??).

An in-depth analysis of the C1s XPS spectrum of sample **1** (see Figure 14) reveals the relative concentration of carbon species (see table in Figure 14).
450 As in the case of the nickel substrates, graphitic carbon (sp^2 at 284.6 eV BE, 61.8%) is dominant, plus diamond-like carbon (sp^3 at 285.2 eV BE, 16.9%), some contribution from oxidized carbon (C-O-C at 286.1 eV BE, 9.7%), and the π - π^* shake-up satellite (at 289.4 eV BE, 11.6%). Taking these numbers into account, the C1s XPS spectrum of graphene nano-sheets is closer to that
455 of the early stages of graphene growth on Ni(111) as compared to the C1s XPS results of graphene on Ni foil. This can be expected from the large amount of defects and graphene sheet edges visible in the SEM images of both of the former sample systems as compared to the latter graphene sample **3** on Ni foil.

Comparing the above results with previous studies on the PE-CVD growth
460 of vertical graphene nano-sheets, we would like to point out that this could be achieved without the use of either a surface catalyst or an electric field (perpendicular to the sample surface) as typically generated by the plasma sheath

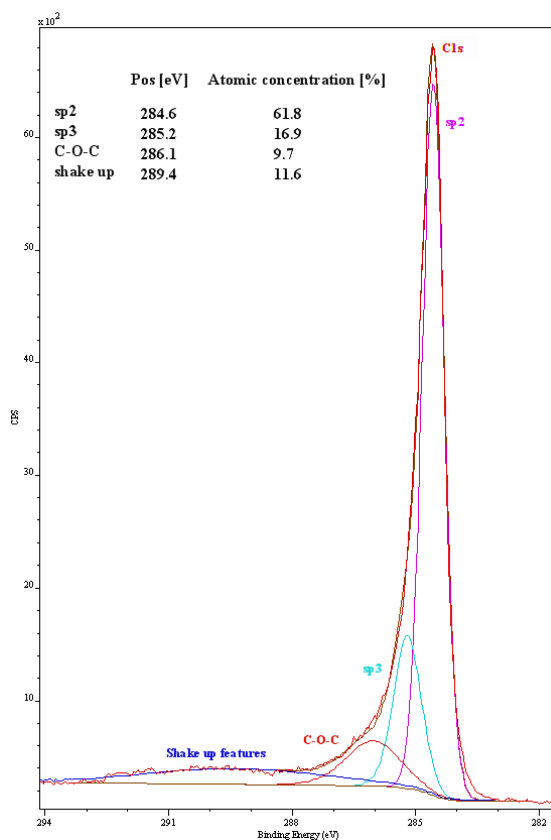


Figure 14: C1s XPS line of the graphene on HOPG(0001) sample *1*, and fitting its different components (sp^2 , sp^3 , C-O-C and *shake up features*). Inset: XPS overview spectrum of graphene/HOPG(0001) sample *1*. Table insert: Measured positions of the peaks corresponding to the different components in sample *1*, and their relative atomic concentration.

and thus inherent to many other commonly used *direct* plasma PE-CVD setups. While the former catalyst-free nano-sheet growth could already be demonstrated
 465 by several groups (see, e.g., [8, 29, 30]), these processes did rely on the inherent occurrence of an electric field as given by the direct sample exposure of the sample within the PE-CVD setup. In our case, the plasma source is remote with respect to the deposition chamber and thus the electromagnetic fields normal to the sample substrate as created by the plasma source - that could possibly
 470 induce a preferential growth direction as in the case of a classical CCP or direct

plasma ICP setup [8] - should be minimized. At this point, the most plausible explanation for this finding is that the upper deposition limit for a 2D epitaxial deposition was reached for sample **1** due to the extremely long deposition time of 180 minutes, thus leading to a saturation of the 2D growth parallel to the substrate plane as in HOPG sample **2**, thus initiating a vertical growth of graphene nano-sheets. This is corroborated by the experimental findings of Zhu et al. [8], where the authors propose a initial planar graphene growth on Si and an onset of vertical sheet growth after the deposition of a 1 to 15 nm flat graphene layer (within 8 min at 40% CH_4 in H_2 , 100 mTorr, 680°C sample temperature, and 900 W RF power), when a sufficient level of force develops at the graphene sheet boundaries to curl the leading edge of the top layers upward. Their underlying growth model is based on the production of atomic hydrogen in their ICP plasma, plus the above vertical electric field in conjunction with the polarizability of the graphene sheets. The plasma feedstock gas mixture and substrate temperature used in our experiments do bear some similarity in view of the plasma chemistry, whereas the deposition pressure and RF power are at variance by about one order of magnitude - which may account for the large variation in deposition time (i.e., 8 min versus 180 min). Nevertheless, the major difference is given by the occurrence (or non-occurrence) of a significant perpendicular electric field, thus suggesting a different mechanism underlying the initiation of the vertical growth mode as the one proposed by Zhu et al. [8].

4. Conclusions

We have successfully implemented and used a newly developed *remote inductively coupled low-pressure RF plasma source for the synthesis of multilayer micro-crystalline graphene* on polycrystalline nickel foil and Ni(111) by means of remote plasma-enhanced chemical vapor deposition (rPE-CVD). Also, the catalyst- and field-free growth of *vertical* graphene nano-sheets has been achieved on HOPG(0001).

For the graphene/Ni foil samples, Raman spectroscopy revealed the pre-

500 dominance of an ordered sp^2 growth process with an extremely low amount of defects over a wide surface area, as evidenced by sharp G and D peaks as well as STM analysis. Raman spectra also did yield a first qualitative evidence of the multilayer nature of our samples, as witnessed by the low 2D/G ratio. The graphene thickness was quantitatively established to be close to six graphene
505 monolayers, using the ratio between Ni2p and C1s peaks in the XPS spectra. On Ni foils, the addition of a small amount ($\sim 20\%$) of H_2 into the plasma feedstock gas mixture turns out to be crucial to reduce the growth of a disordered sp^3 or amorphous sp^3/sp^2 carbon phases. So far, substrate temperatures slightly above $700^\circ C$ and RF powers of $\sim 200W$ have proven to be optimum, in
510 contrast to lower values that lead to an insufficient growth rate for the specific case of a Ni foil substrate. Moreover, a deposition time of 3 to 5 *min* for 6 graphene monolayers at gas pressures of 0.1 *mbar* did yield our best results in view of the growth of defect-free large area graphene layers. Lower deposition times are inefficient, whereas lower pressures do enhance the deposition rate,
515 thereby resulting in an excessive growth of thick graphene films together with an enhanced density of defects.

Polycrystalline Ni foils have so far been the most promising substrates to perform plasma-assisted depositions of graphene, as they yield a growth of 2-dimensional multilayers. Even though we have so far not tested a fine control
520 over the number of deposited layers, this could be easily achieved in the near future by means of performing dedicated deposition runs following the already established procedures. The rPE-CVD graphene samples synthesized on the Ni foils have proven to be good candidates for *STM* analysis, yielding a fairly complete picture of the produced layers via the imaging of the carbon atoms
525 contained in the graphene lattice. In more detail, large defect-free graphene areas could be demonstrated together with smooth transitions between substrate defects as well as areas with different graphene stacking modes.

A catalyst- and field-free homogeneous coverage of *vertical* graphene nano-sheets was successfully achieved on HOPG(0001). **To our knowledge, this**
530 **could be achieved under catalyst- and field-free conditions for the**

first time. SEM images did show a clear perpendicular growth due to a combination of deposition rate and extended deposition time, resulting into the aforementioned vertical graphene nano-sheets. Based on a comparison with similar results from the PE-CVD literature, we would like to point out the existence
535 of a transition from an in-plane to a vertical growth mode together with the use of atomic hydrogen within the plasma. However, we see no direct evidence for the need of significant electric fields perpendicular to the sample surface **or of surface catalysts** to enable the growth of vertical graphene nano-sheets. Working on the hypothesis of long deposition times leading to a vertical growth,
540 further rPE-CVD studies are needed in order to elucidate the detailed dynamics regarding the transition between the in-plane and the vertical growth modes of graphene nano-sheets on HOPG(0001).

**Summarizing the above results, the GV10x rPE-CVD downstream (or afterglow) plasma source appears to be a promising tool for the
545 deposition of graphene micro- and nanostructures as well as for the more complex *in situ* UHV preparation of, e.g., multi-layered hybrid graphene sample systems.**

5. Acknowledgments

We acknowledge support by expert staff of ibss Group Inc. We also acknowl-
550 edge the scientific advice by S. Ferrer (CELLS) and the contribution by the CELLS technical staff, especially L. Ginés, as well as the friendly collaboration of M.Panighel, N.Domingo, and A.Verdaguer (ICN2) during the sample characterization activities. A. R. G. thanks the Spanish Ministry of Economy and Competitiveness (MINECO) for its support through Grant No. CSD2010-00044
555 (Consolider NANOTHERM). The work at ICMAB (Raman measurements) was carried out under the auspices of the Spanish Severo Ochoa Centre of Excellence program (grant SEV-2015-0496). SEM, STM, and XPS measurements were performed at ICN2 that acknowledges support from the Severo Ochoa Program (MINECO, Grant SEV-2013-0295). PEEM and LEEM measurements

560 were performed at the Circe beamline of the ALBA synchrotron light facility
with the assistance of CELLS-ALBA staff. E. Pach is enrolled in the PhD
program in Materials Sciences at the UAB.

References

- [1] Y. B. Zhang, Y. W. Tan, H. L. Stormer, P. Kim, Experimental observa-
565 tion of the quantum Hall effect and Berry's phase in graphene, *Nature*
438 (7065) (2005) 201–204. doi:10.1038/nature04235.
- [2] T. Ohta, Controlling the Electronic Structure of Bilayer Graphene, *Science*
313 (5789) (2006) 951–954. doi:10.1126/science.1130681.
- [3] D. Boyd, W.-H. Lin, C.-C. Hsu, M. Teague, C.-C. Chen, Y.-Y. Lo, W.-Y.
570 Chan, W.-B. Su, T.-C. Cheng, C.-S. Chang, C.-I. Wu, N.-C. Yeh, Single-
step deposition of high-mobility graphene at reduced temperatures, *Nature*
Communications 6 (2015) 6620. doi:10.1038/ncomms7620.
URL <http://www.nature.com/doifinder/10.1038/ncomms7620>
- [4] G. Nandamuri, S. Roumimov, R. Solanki, Remote plasma assisted growth
575 of graphene films, *Appl. Phys. Lett.* 96 (15) (2010) 154101. doi:10.1063/
1.3387812.
- [5] J. Kim, M. Ishihara, Y. Koga, K. Tsugawa, M. Hasegawa, S. Iijima, Low-
temperature synthesis of large-area graphene-based transparent conductive
films using surface wave plasma chemical vapor deposition, *Appl. Phys.*
580 *Lett.* 98 (9) (2011) 091502. doi:10.1063/1.3561747.
- [6] L. Zhang, Z. Shi, Y. Wang, R. Yang, D. Shi, G. Zhang, Catalyst-free growth
of nanographene films on various substrates, *Nano Res.* 4 (3) (2011) 315–
321. doi:10.1007/s12274-010-0086-5.
- [7] L. Zhang, Z. Shi, D. Liu, R. Yang, D. Shi, G. Zhang, Vapour-phase
585 graphene epitaxy at low temperatures, *Nano Res.* 5 (4) (2012) 258–264.
doi:10.1007/s12274-012-0205-6.

- [8] M. Zhu, J. Wang, B. C. Holloway, R. Outlaw, X. Zhao, K. Hou, V. Shutthanandan, D. M. Manos, A mechanism for carbon nanosheet formation, *Carbon* N. Y. 45 (11) (2007) 2229–2234. doi:10.1016/j.carbon.2007.06.017.
- 590
- [9] CELLS - ALBA Synchrotron Light Source.
URL <http://www.cells.es>
- [10] ibss Group Inc., URL <http://www.ibssgroup.com>.
- [11] E. Pellegrin, I. Šics, J. Reyes-Herrera, C. Perez Sempere, J. J. Lopez Alcolea, M. Langlois, J. Fernandez Rodriguez, V. Carlino, Characterization, optimization and surface physics aspects of in situ plasma mirror cleaning, *J. Synchrotron Radiat.* 21 (2) (2014) 300–314. doi:10.1107/S1600577513032402.
- 595
- [12] M. G. Cuxart, J. Reyes-Herrera, I. Šics, A. R. Goñi, H. M. Fernandez, V. Carlino, E. Pellegrin, Remote plasma cleaning of optical surfaces: Cleaning rates of different carbon allotropes as a function of RF powers and distances, *Appl. Surf. Sci.* 362 (2016) 448–458. doi:10.1016/j.apsusc.2015.11.117.
- 600
- [13] A. Fridman, L. A. Kennedy, *Plasma Physics and Engineering*, 2011.
- [14] Alexander Fridman, *Plasma Chemistry*, 2012.
- 605
- [15] A. C. Ferrari, J. C. Meyer, V. Scardaci, C. Casiraghi, M. Lazzeri, F. Mauri, S. Piscanec, D. Jiang, K. S. Novoselov, S. Roth, A. K. Geim, Raman Spectrum of Graphene and Graphene Layers, *Phys. Rev. Lett.* 97 (18) (2006) 187401. doi:10.1103/PhysRevLett.97.187401.
- [16] PLASUS Specline, PLASUS GmbH, Mering, Germany.
- 610
- [17] W. S. W. S. M. Werner, C. J. Powel, NIST Database for the Simulation of Electron Spectra for Surface Analysis (SESSA), National Institute of Standards and Technology, Gaithersburg, Maryland.

- [18] A. C. Ferrari, D. M. Basko, Raman spectroscopy as a versatile tool for
615 studying the properties of graphene, *Nat. Nanotechnol.* 8 (4) (2013) 235–
246. doi:10.1038/nnano.2013.46.
- [19] C. Thomsen, S. Reich, Double Resonant Raman Scattering in Graphite,
Phys. Rev. Lett. 85 (24) (2000) 5214–5217. doi:10.1103/PhysRevLett.
85.5214.
- [20] A. C. Ferrari, Raman spectroscopy of graphene and graphite: Disorder,
620 electron-phonon coupling, doping and nonadiabatic effects, *Solid State
Commun.* 143 (1-2) (2007) 47–57. doi:10.1016/j.ssc.2007.03.052.
- [21] A. Reina, X. Jia, J. Ho, D. Nezich, H. Son, V. Bulovic, M. S. Dresselhaus,
J. Kong, Large Area , Few-Layer Graphene Films on Arbitrary Substrates
625 by Chemical Vapor Deposition 2009, *Nano Lett.* 9 (2009) 30–35. doi:
10.1021/nl801827v.
- [22] Z. R. Robinson, P. Tyagi, T. M. Murray, C. A. Ventrice, S. Chen, A. Mun-
son, C. W. Magnuson, R. S. Ruoff, Substrate grain size and orientation
of cu and cu-ni foils used for the growth of graphene films, *Journal of
630 Vacuum Science & Technology A* 30 (1) (2012) 23919–23927. doi:http:
//dx.doi.org/10.1116/1.3663877.
URL [http://scitation.aip.org/content/avs/journal/jvsta/30/1/
10.1116/1.3663877](http://scitation.aip.org/content/avs/journal/jvsta/30/1/10.1116/1.3663877)
- [23] A. C. Ferrari, J. Robertson, Raman spectroscopy of amorphous, nanos-
635 tructured, diamond-like carbon, and nanodiamond, *Philos. Trans. R. Soc.
A Math. Phys. Eng. Sci.* 362 (1824) (2004) 2477–2512. doi:10.1098/rsta.
2004.1452.
- [24] NIST Atomic Spectra Database Version 2.0., Gaithersburg, Maryland, Na-
tional Institute of Standards and Technology.
- [25] T. L. Burnett, R. Yakimova, O. Kazakova, Identification of epitaxial
640 graphene domains and adsorbed species in ambient conditions using quan-

tified topography measurements, *J. Appl. Phys.* 112 (5) (2012) 054308.
doi:10.1063/1.4748957.

[26] F. Bianchini, L. L. Patera, M. Peressi, C. Africh, G. Comelli, Atomic Scale
645 Identification of Coexisting Graphene Structures on Ni(111), *J. Phys.*
Chem. Lett. (5) (2014) 467–473.

[27] W. Yan, L. Meng, M. Liu, J.-B. Qiao, Z.-D. Chu, R.-F. Dou, Z. Liu, J.-C.
Nie, D. G. Naugle, L. He, Angle-dependent van hove singularities and their
breakdown in twisted graphene bilayers, *Phys. Rev. B* 90 (2014) 115402.
650 doi:10.1103/PhysRevB.90.115402.
URL <http://link.aps.org/doi/10.1103/PhysRevB.90.115402>

[28] I. Horcas, R. Fernandez, J. M. Gomez-Rodriguez, J. Colchero, J. Gomez-
Herrero, A. M. Baro, Wsxn: A software for scanning probe microscopy
and a tool for nanotechnology, *Review of Scientific Instruments* 78 (1).
655 doi:http://dx.doi.org/10.1063/1.2432410.
URL [http://scitation.aip.org/content/aip/journal/rsi/78/1/10.](http://scitation.aip.org/content/aip/journal/rsi/78/1/10.1063/1.2432410)
1063/1.2432410

[29] J. Wang, M. Zhu, R. Outlaw, X. Zhao, D. Manos, B. Holloway, Synthesis of
carbon nanosheets by inductively coupled radio-frequency plasma enhanced
660 chemical vapor deposition, *Carbon N. Y.* 42 (14) (2004) 2867–2872. doi:
10.1016/j.carbon.2004.06.035.

[30] J. J. Wang, M. Y. Zhu, R. A. Outlaw, X. Zhao, D. M. Manos, B. C.
Holloway, V. P. Mammana, Free-standing subnanometer graphite sheets,
Applied Physics Letters 85 (7) (2004) 1265–1267. doi:http://dx.doi.
665 org/10.1063/1.1782253.
URL [http://scitation.aip.org/content/aip/journal/apl/85/7/10.](http://scitation.aip.org/content/aip/journal/apl/85/7/10.1063/1.1782253)
1063/1.1782253

Fig. 1

[Click here to download high resolution image](#)

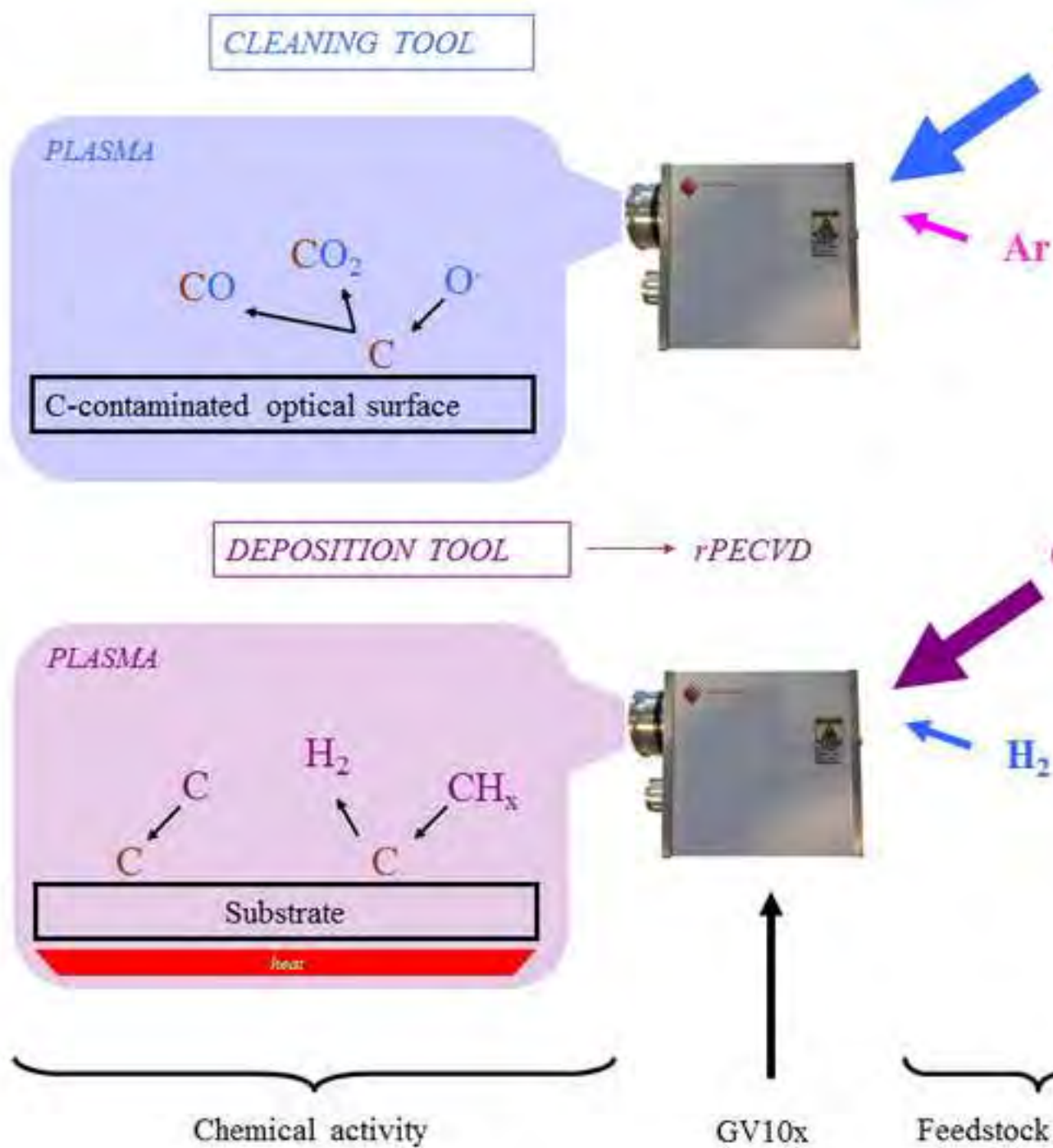


Fig. 2

[Click here to download high resolution image](#)

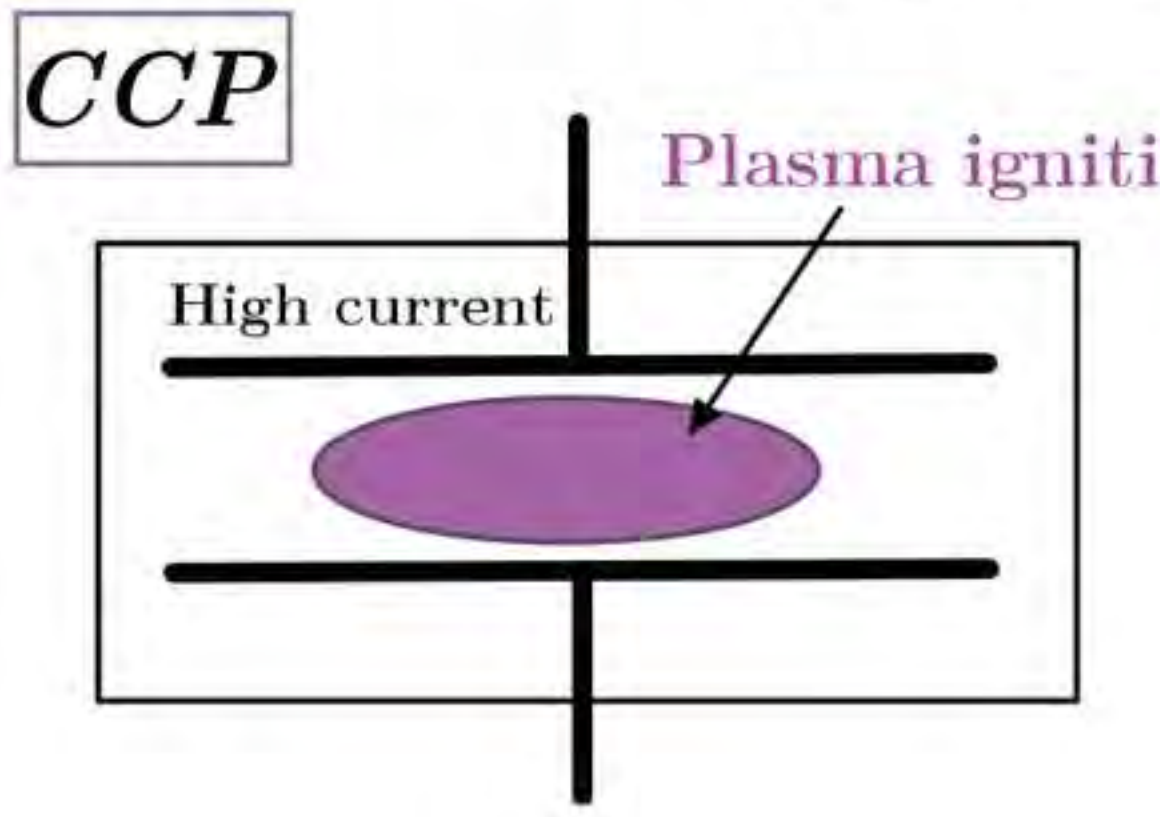
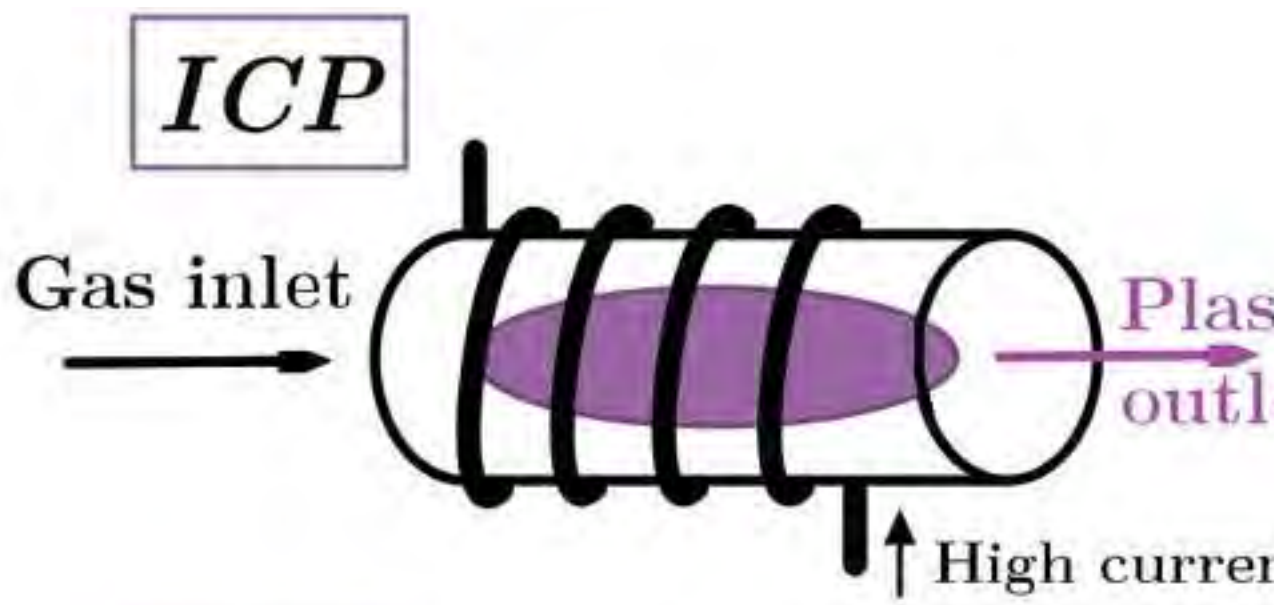


Fig. 3

[Click here to download high resolution image](#)

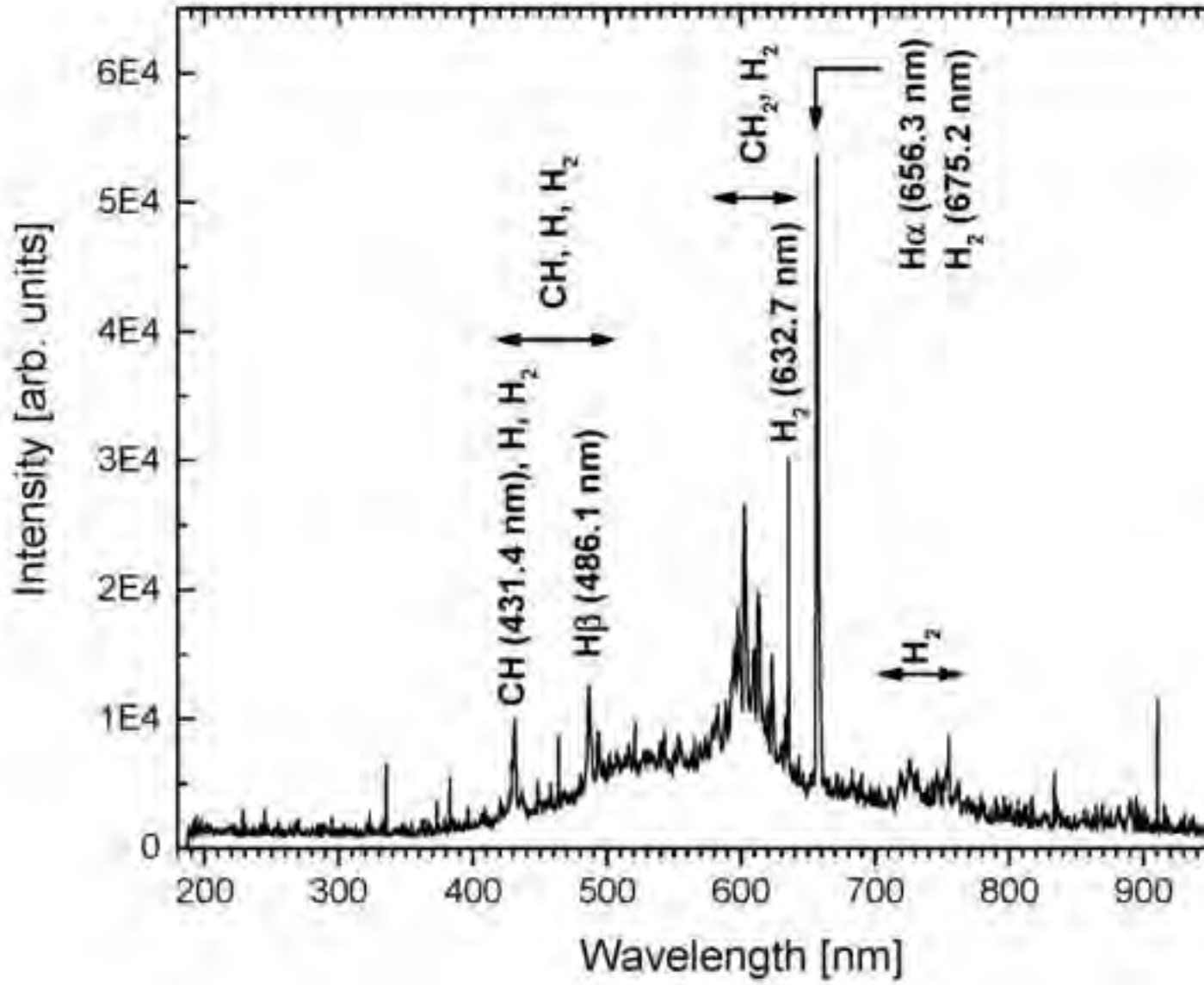


Fig. 4a

[Click here to download high resolution image](#)

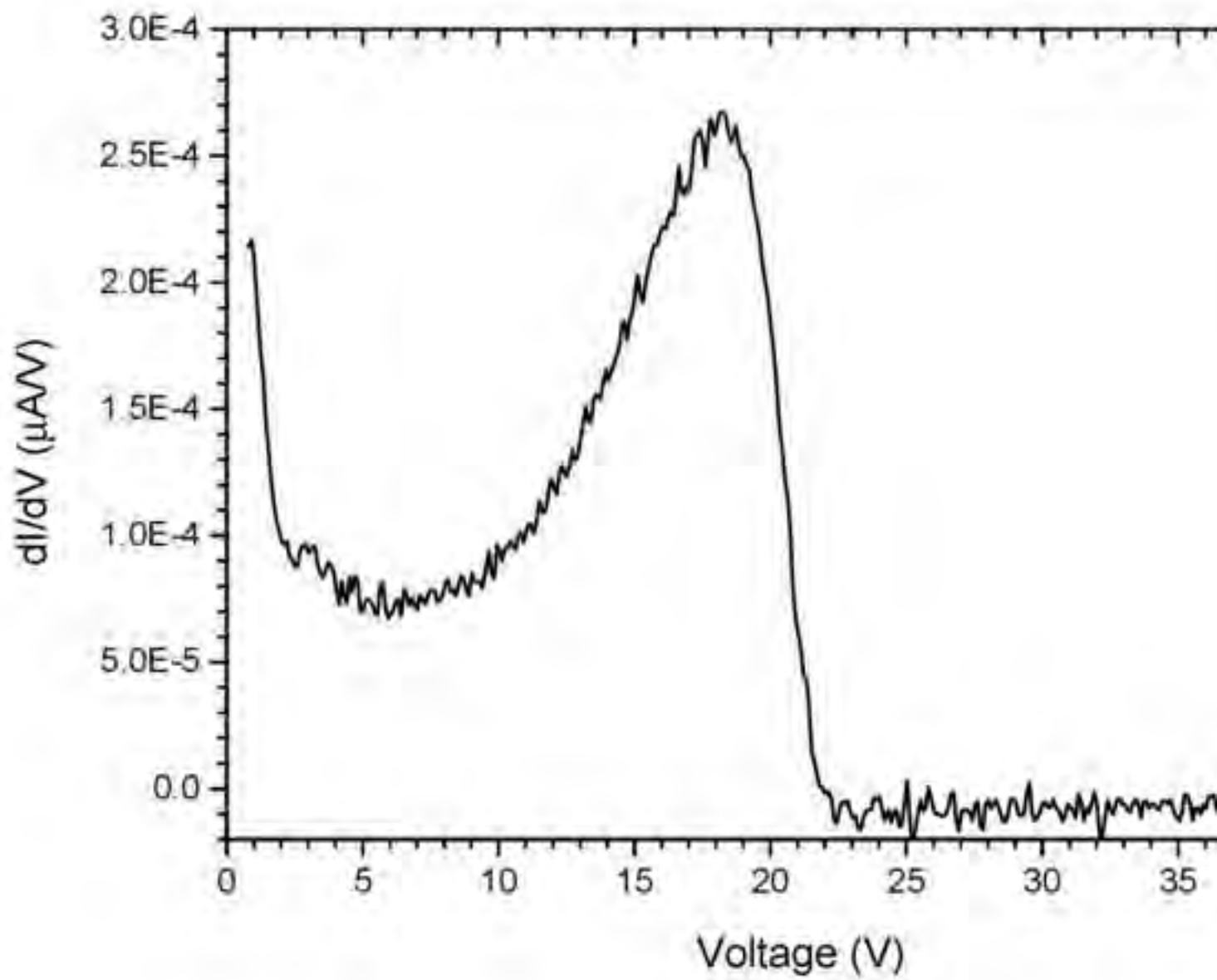


Fig. 4b

[Click here to download high resolution image](#)

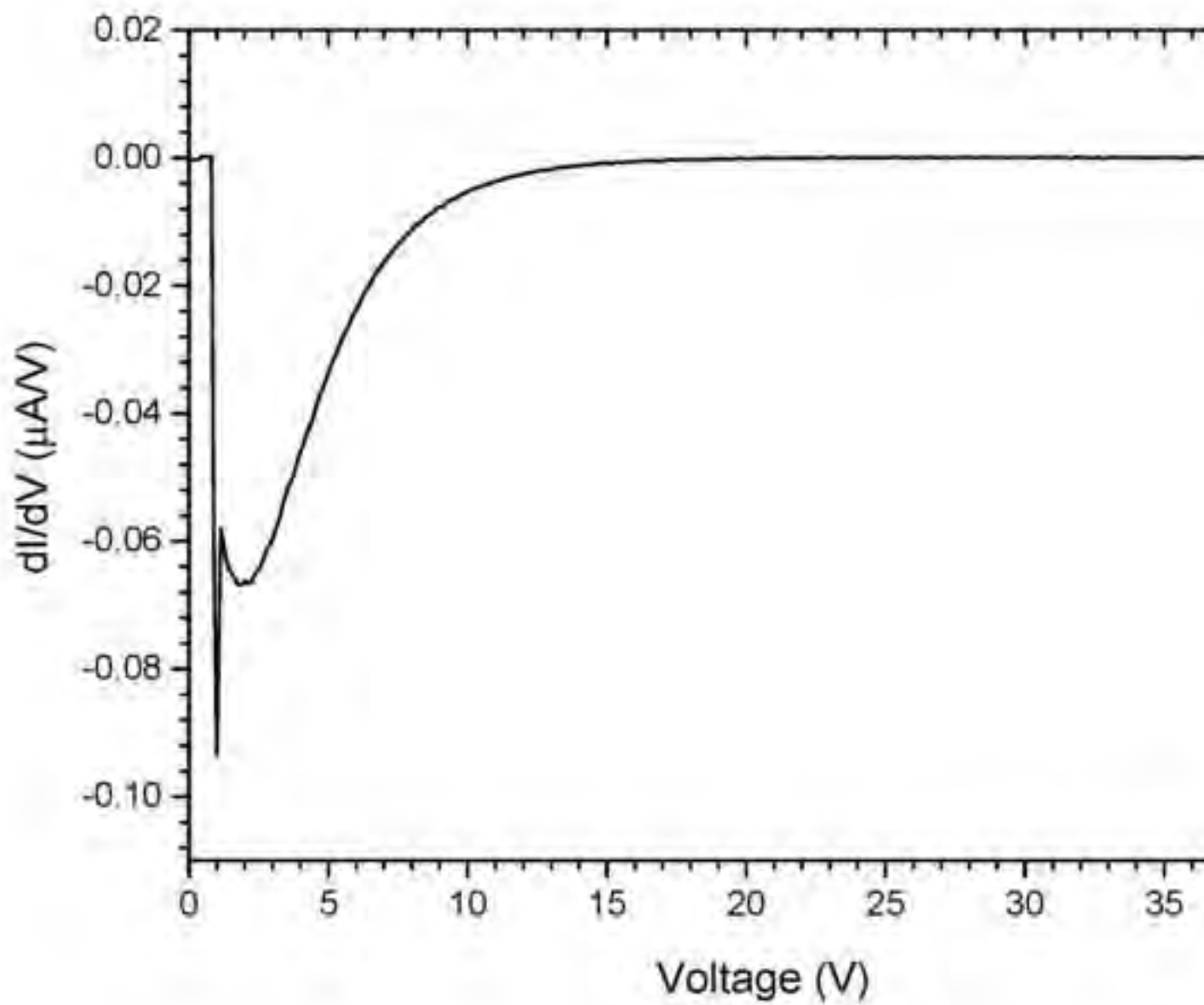


Fig. 5

[Click here to download high resolution image](#)

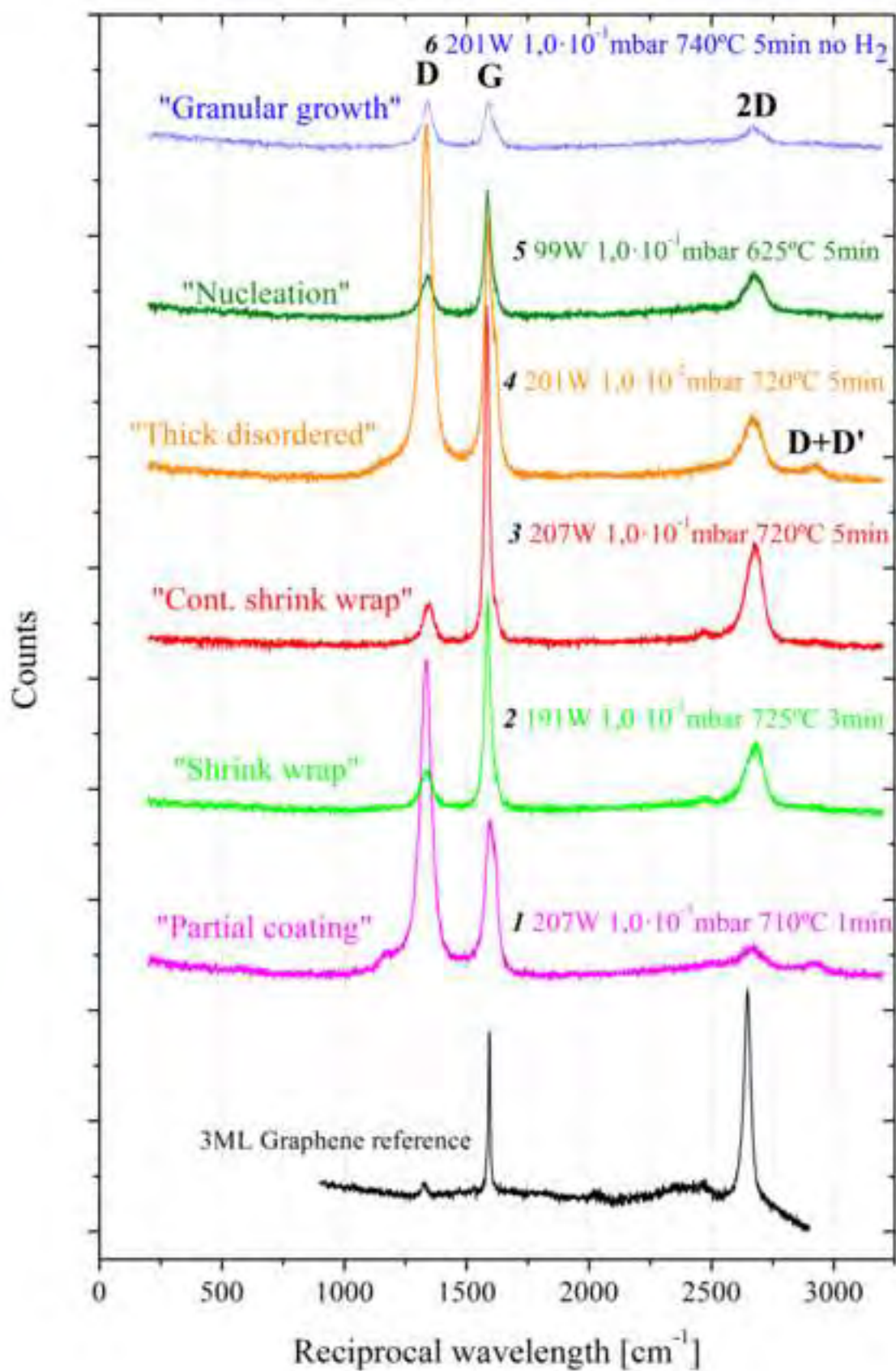


Fig. 6a

[Click here to download high resolution image](#)

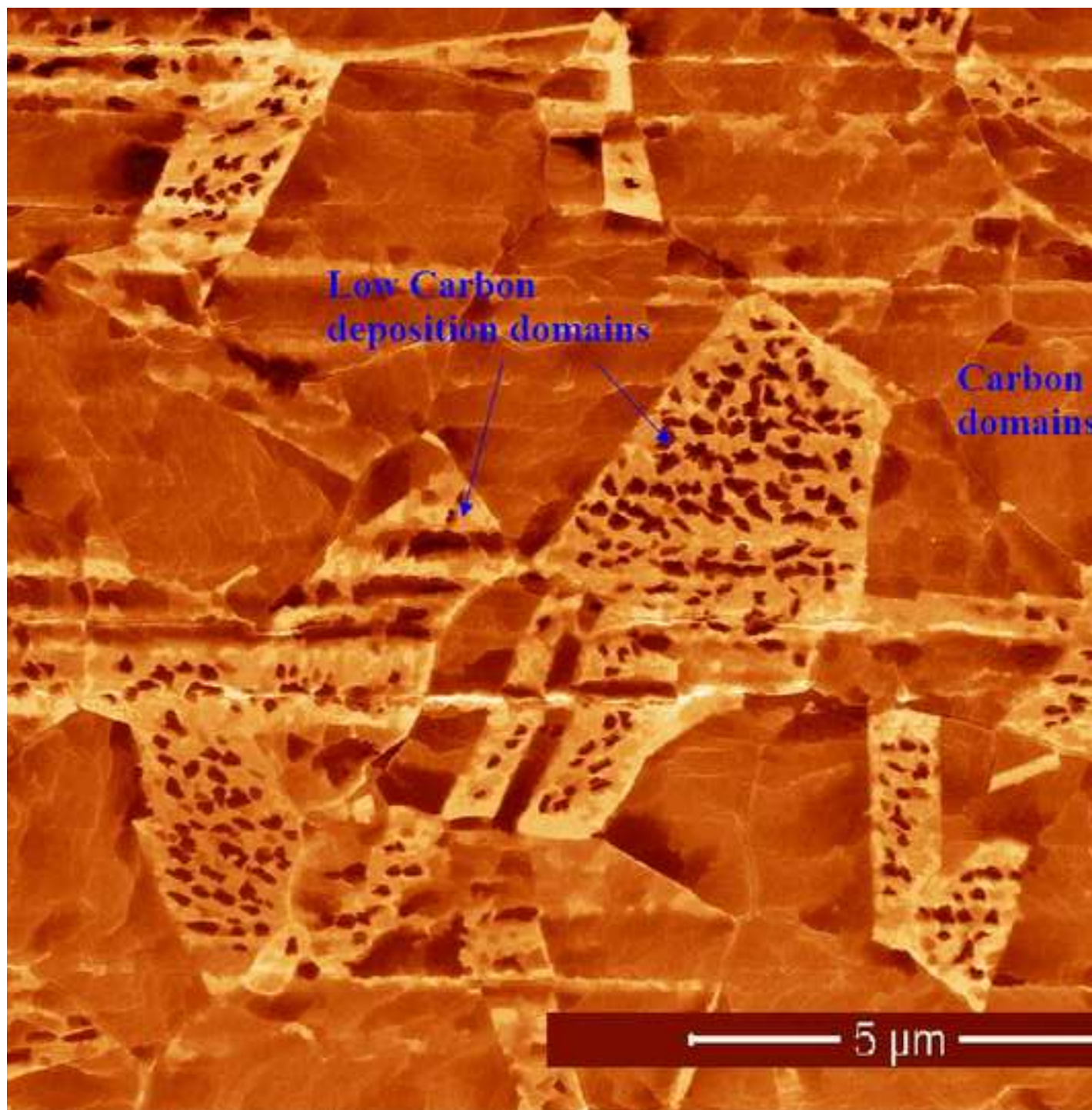


Fig. 6b

[Click here to download high resolution image](#)

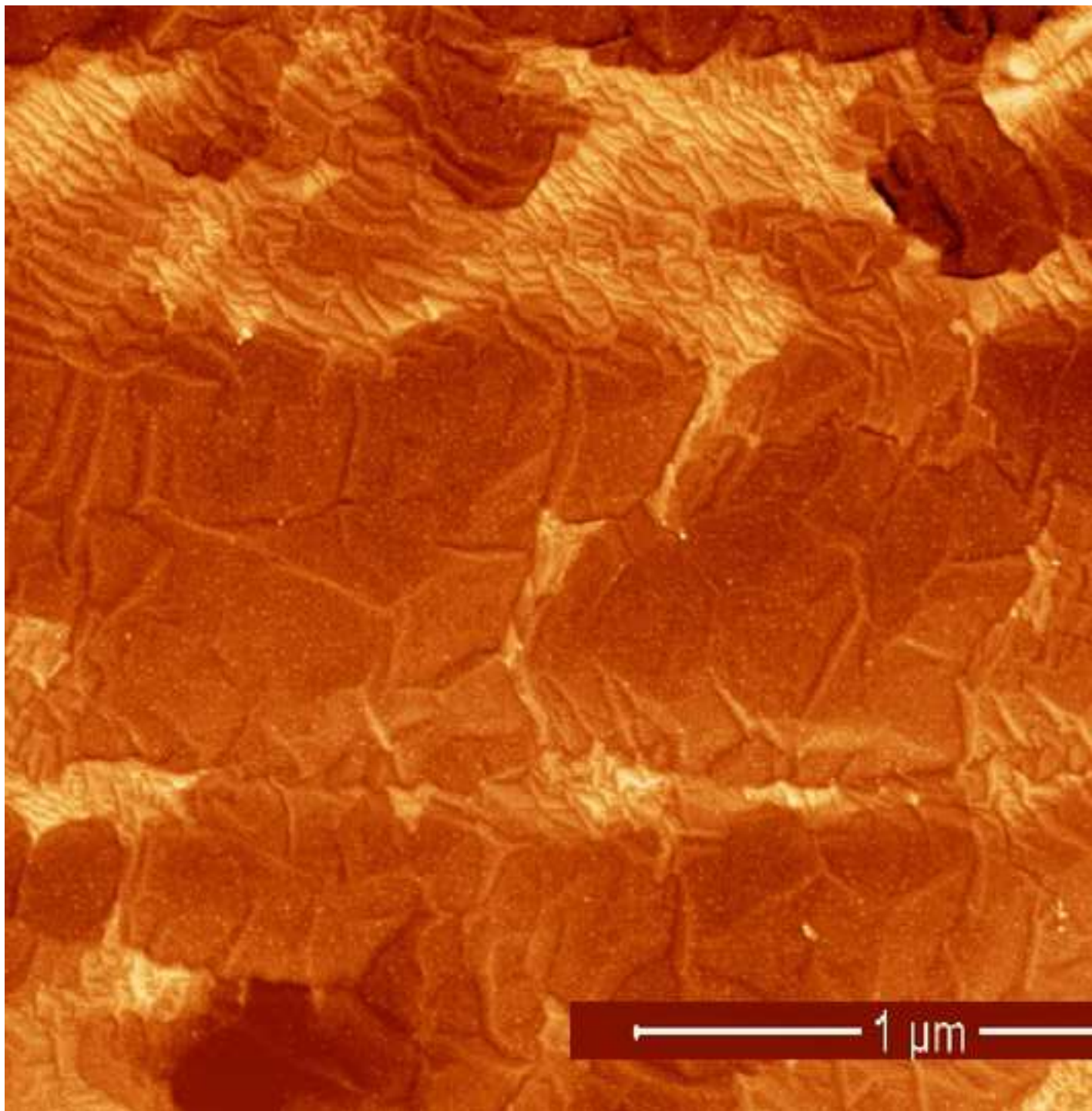


Fig. 6c

[Click here to download high resolution image](#)

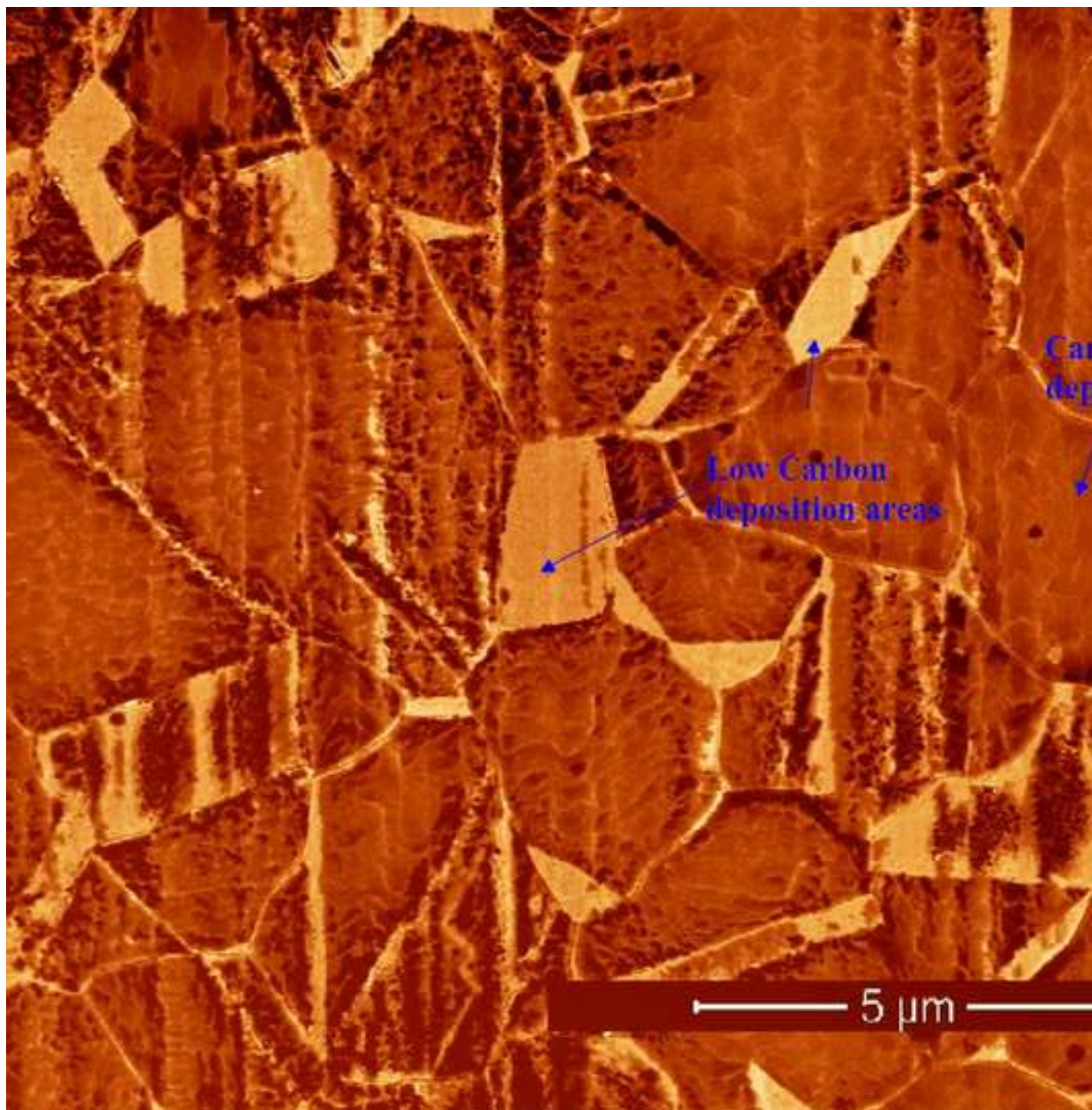


Fig. 6d

[Click here to download high resolution image](#)

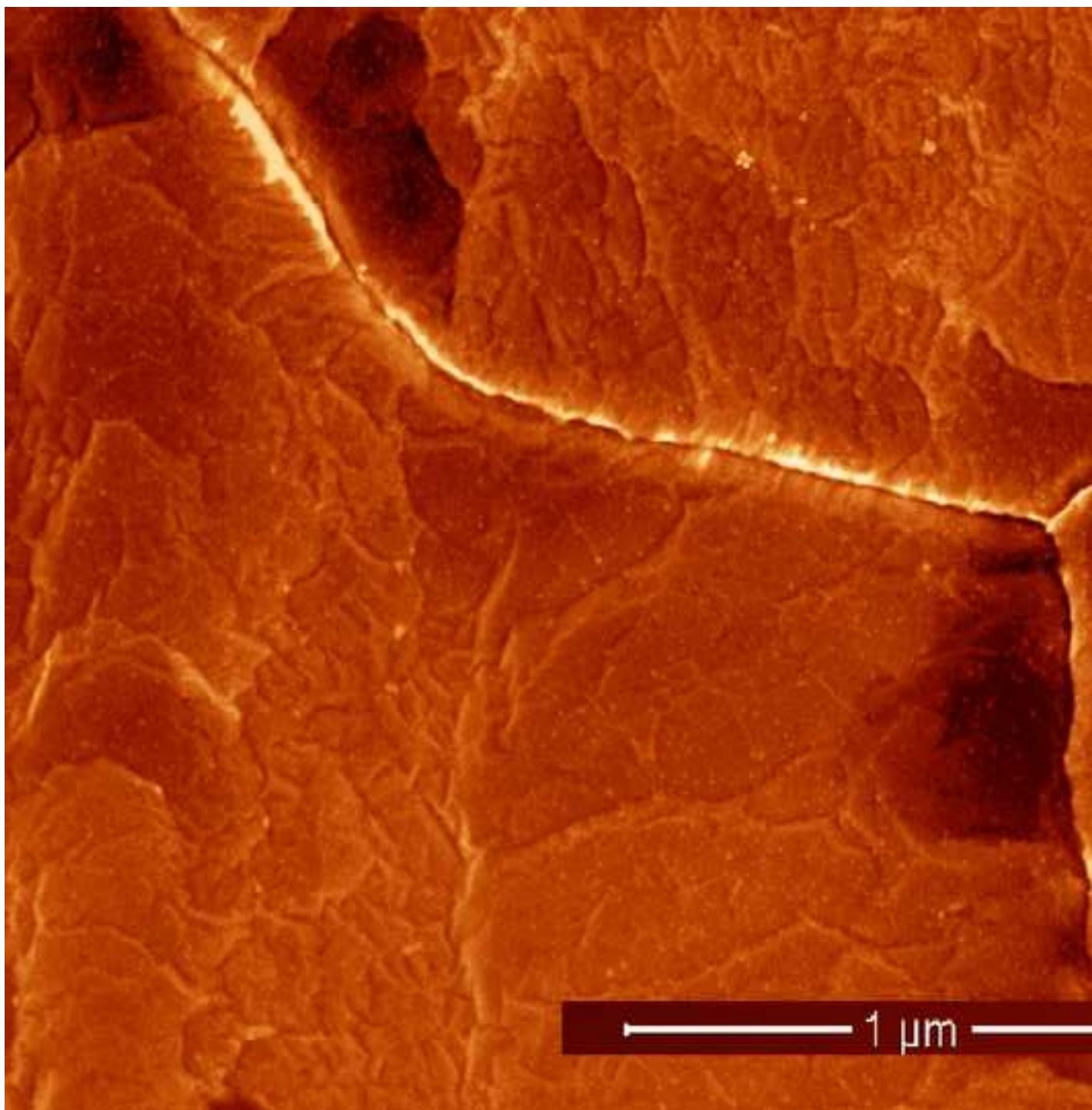


Fig. 6e

[Click here to download high resolution image](#)

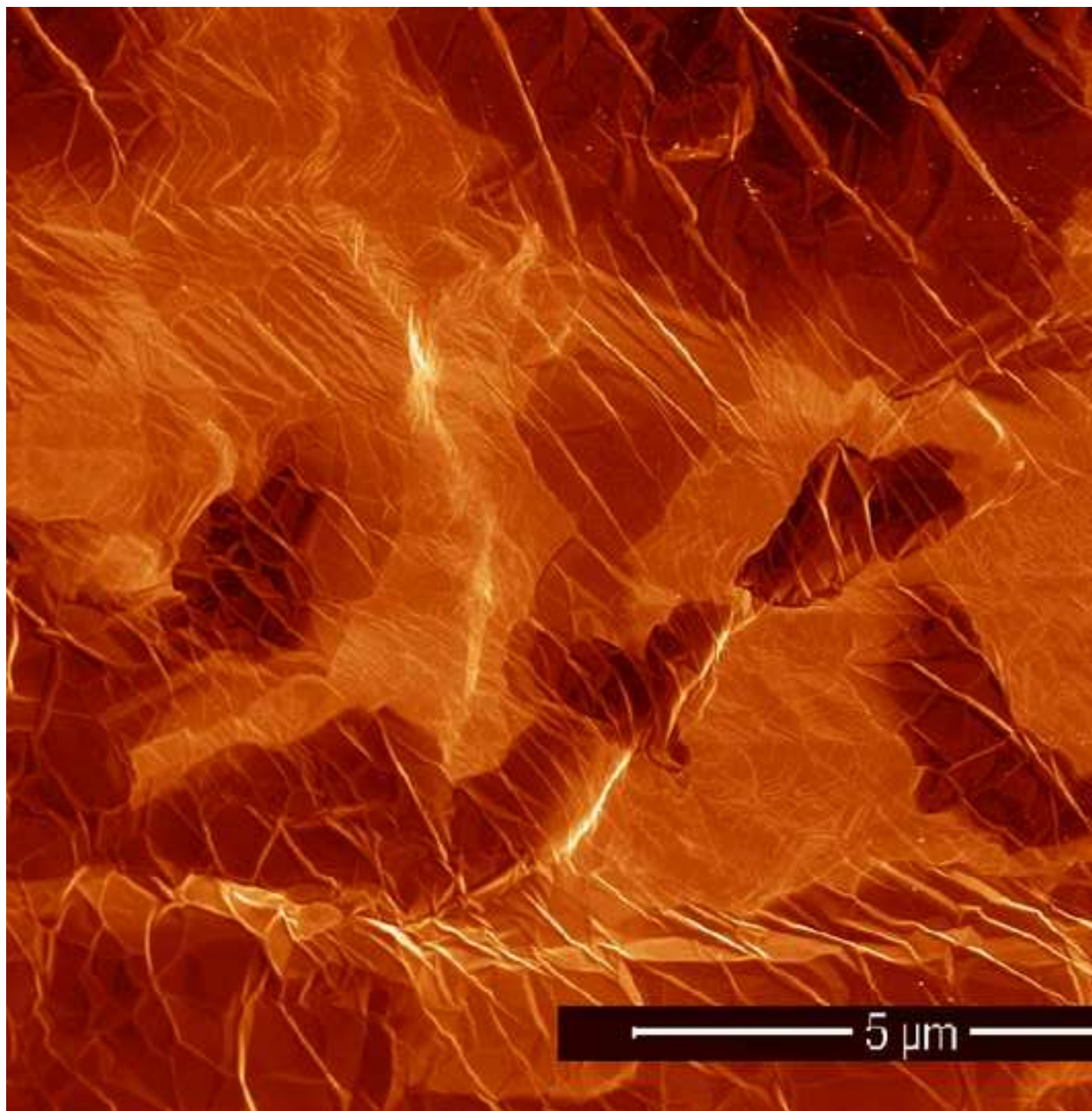


Fig. 6f

[Click here to download high resolution image](#)

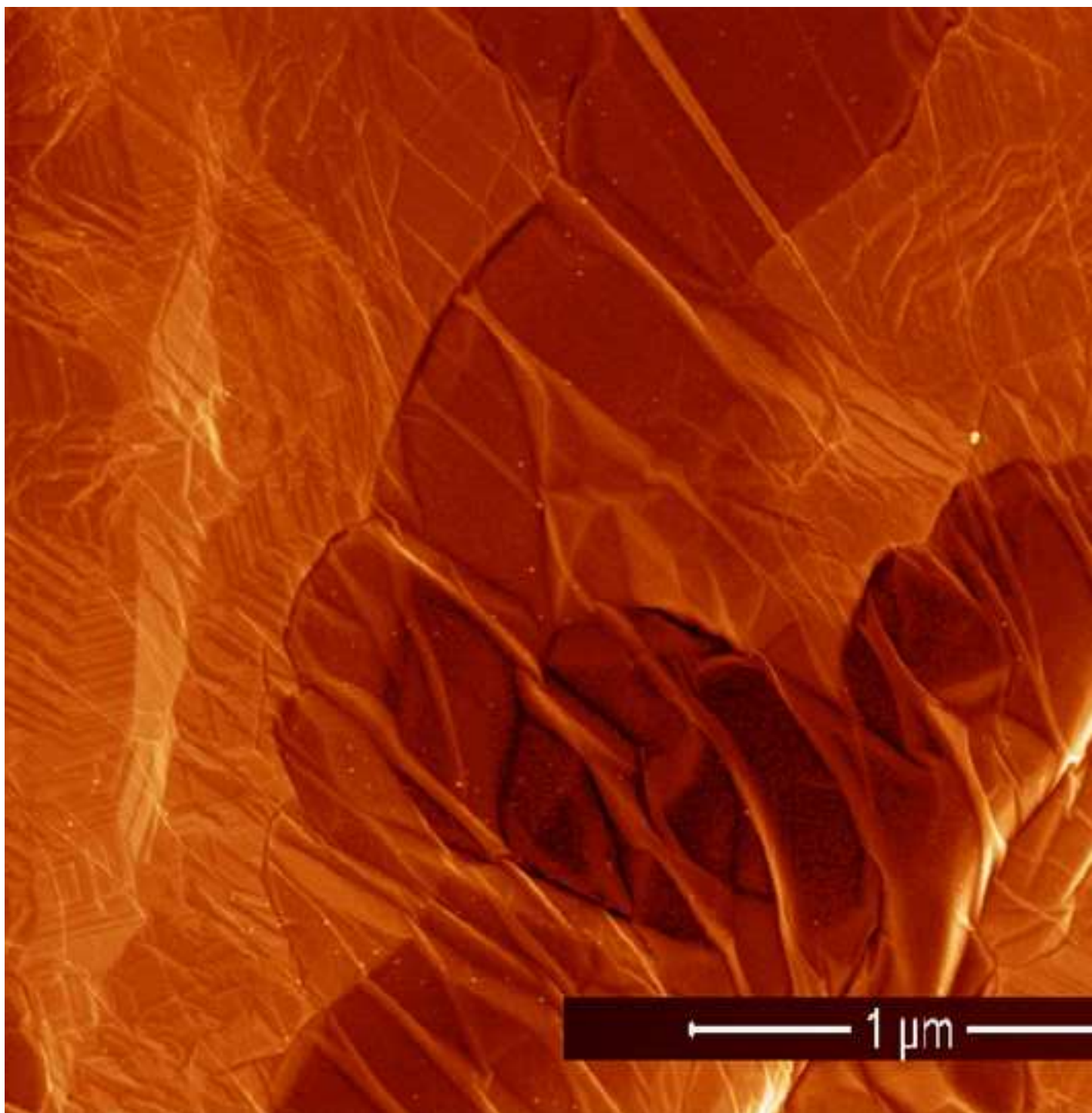


Fig. 7a

[Click here to download high resolution image](#)

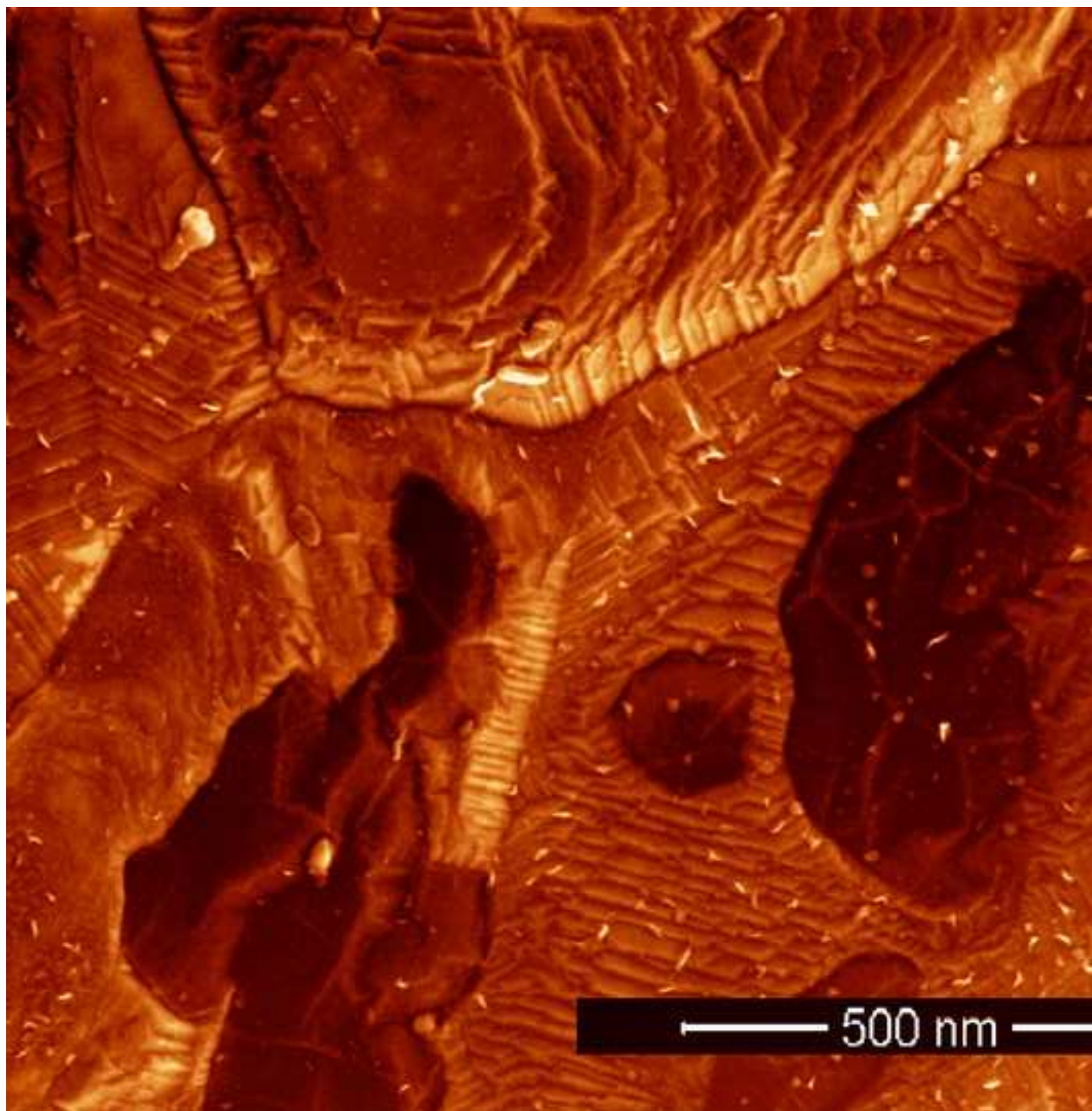


Fig. 7b

[Click here to download high resolution image](#)

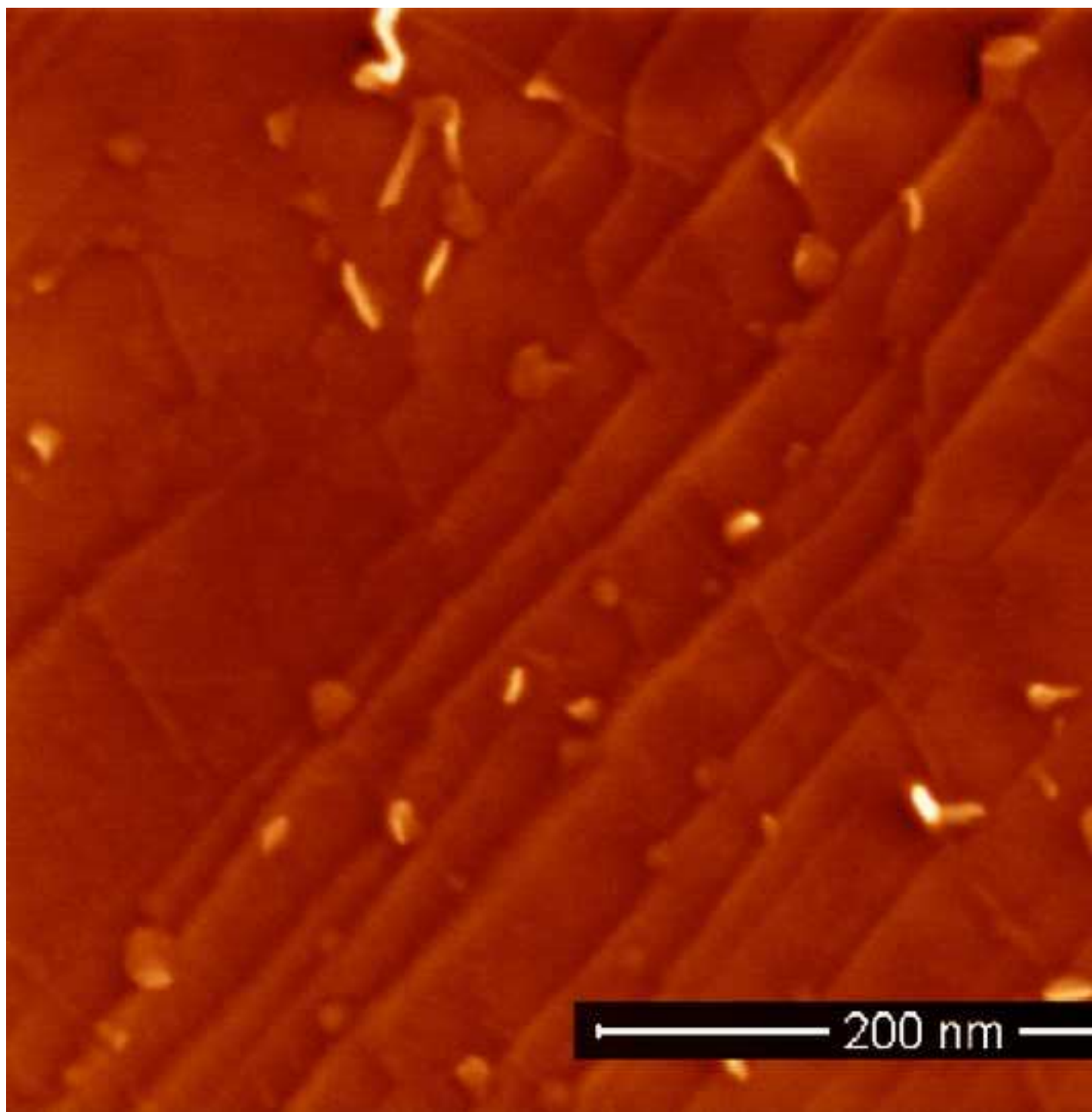


Fig. 7c

[Click here to download high resolution image](#)

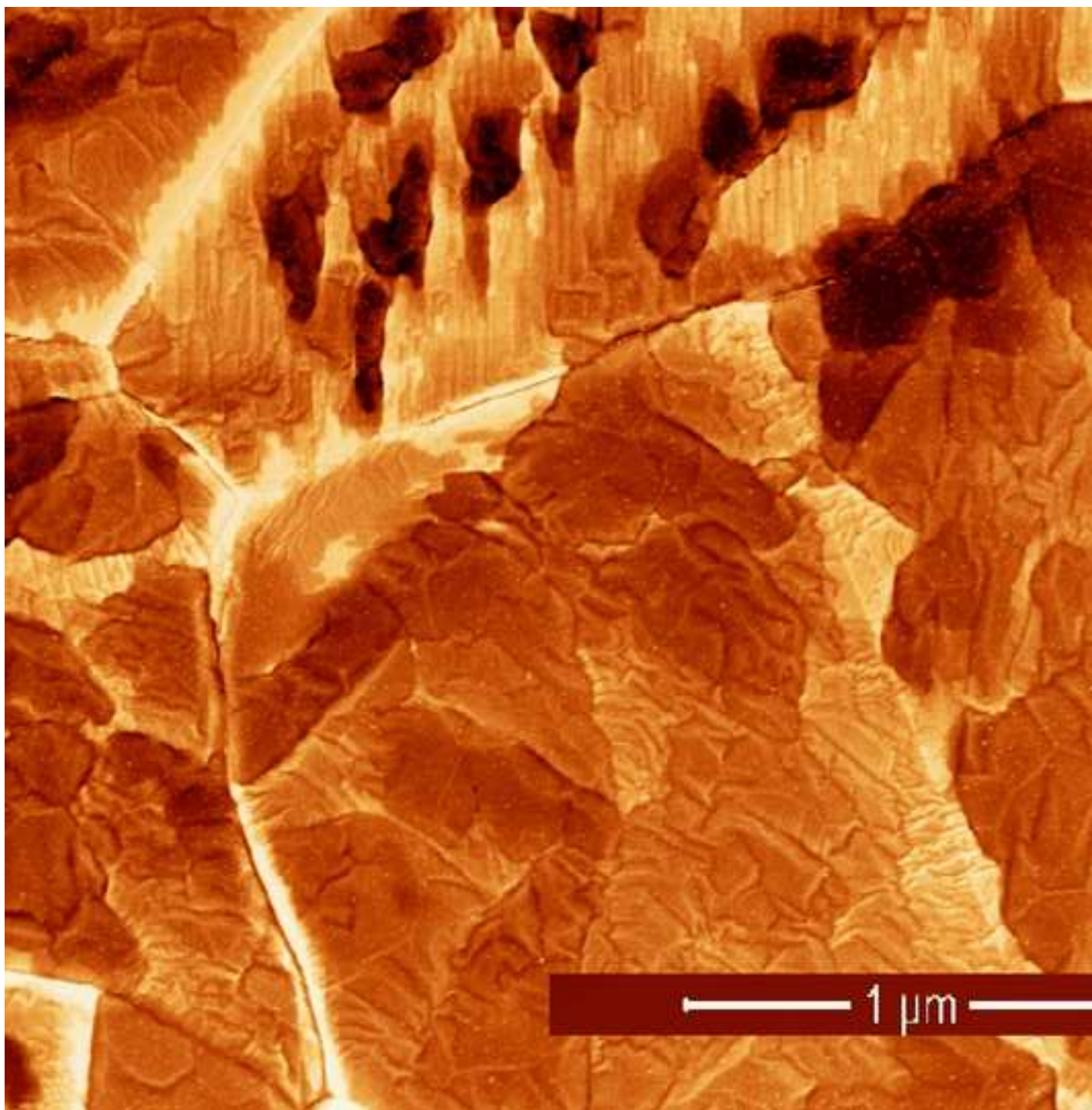


Fig. 7d

[Click here to download high resolution image](#)

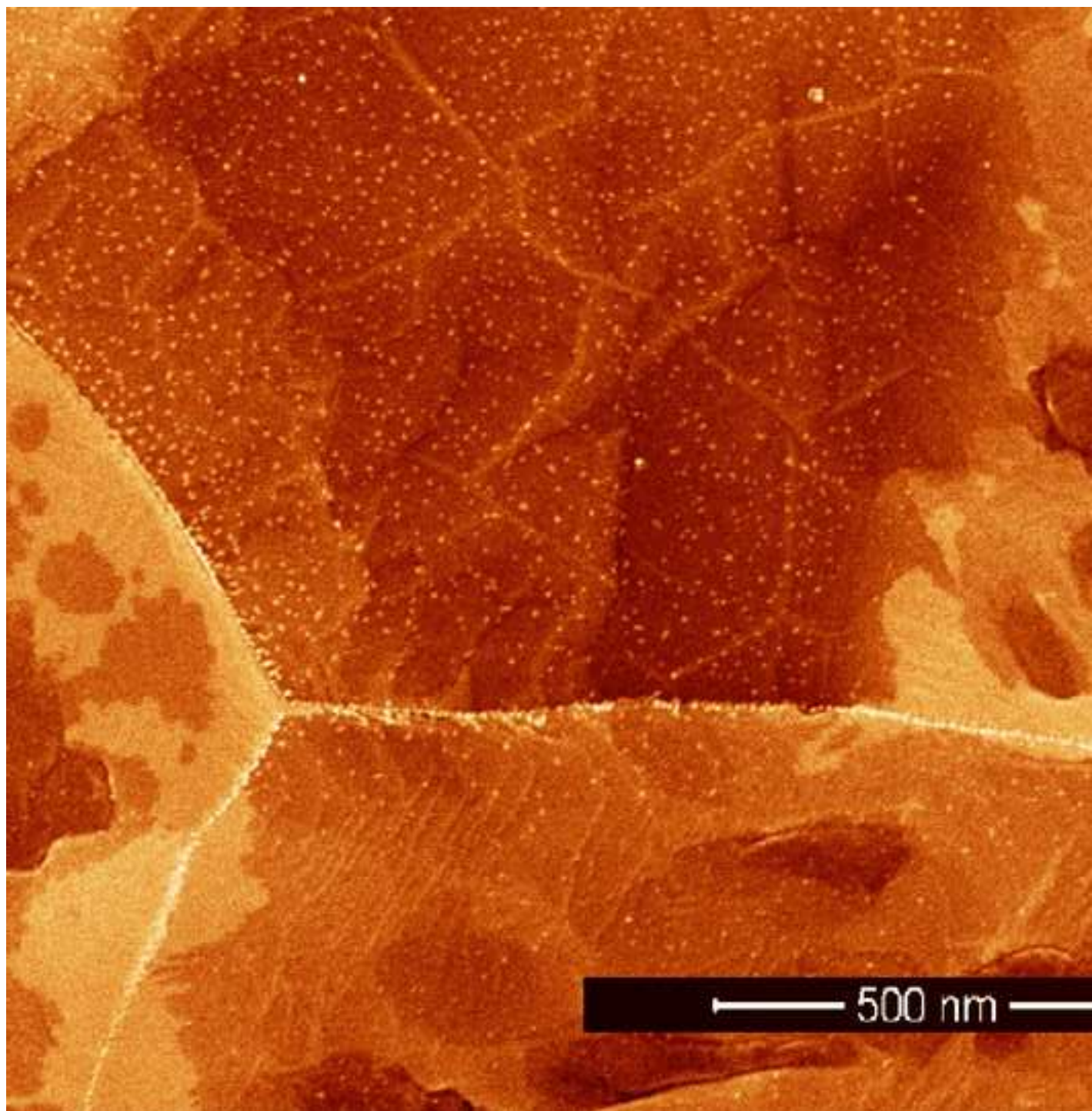


Fig. 7e

[Click here to download high resolution image](#)

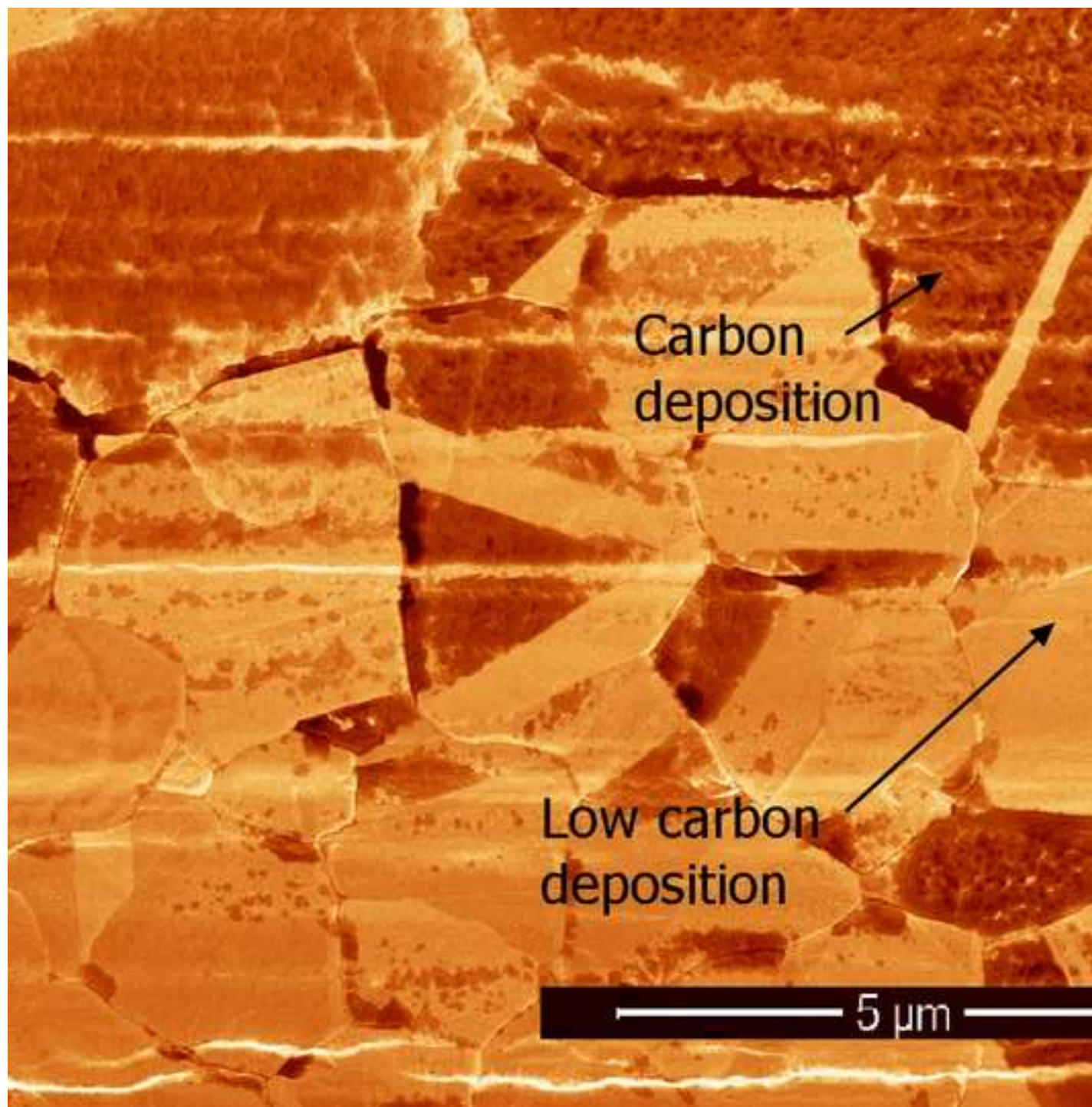


Fig. 7f

[Click here to download high resolution image](#)

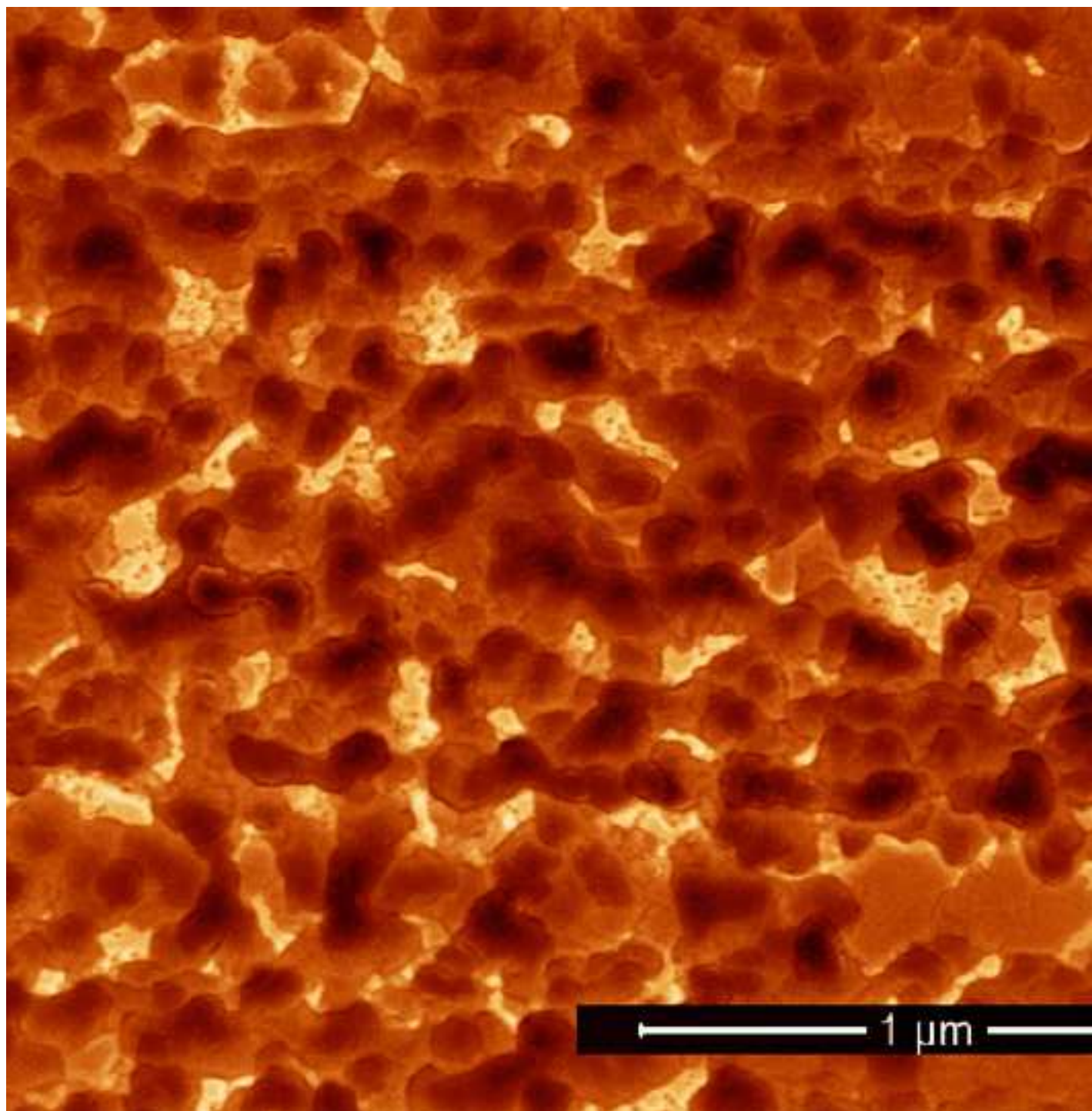


Fig. 8

[Click here to download high resolution image](#)

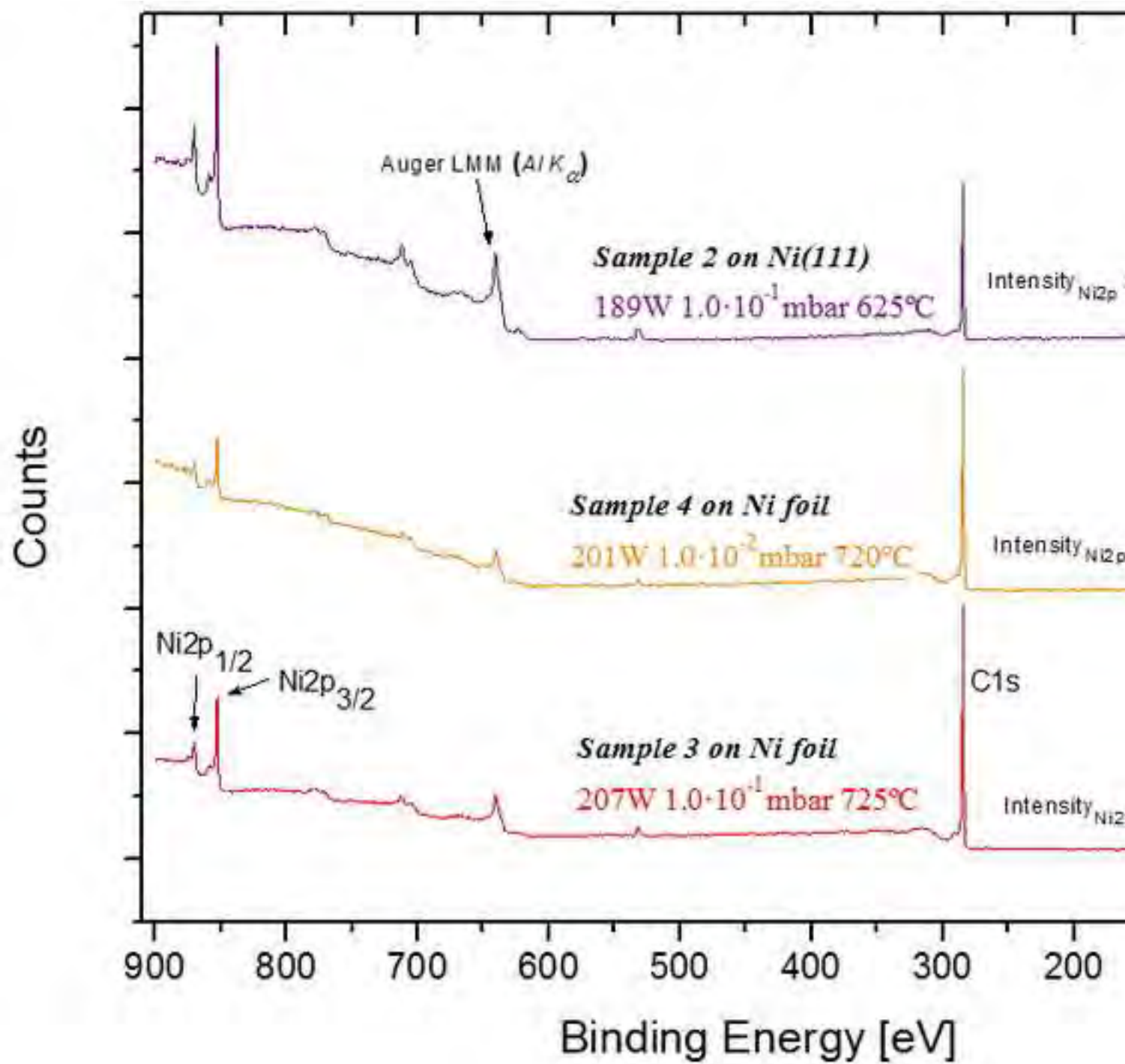


Fig. 9

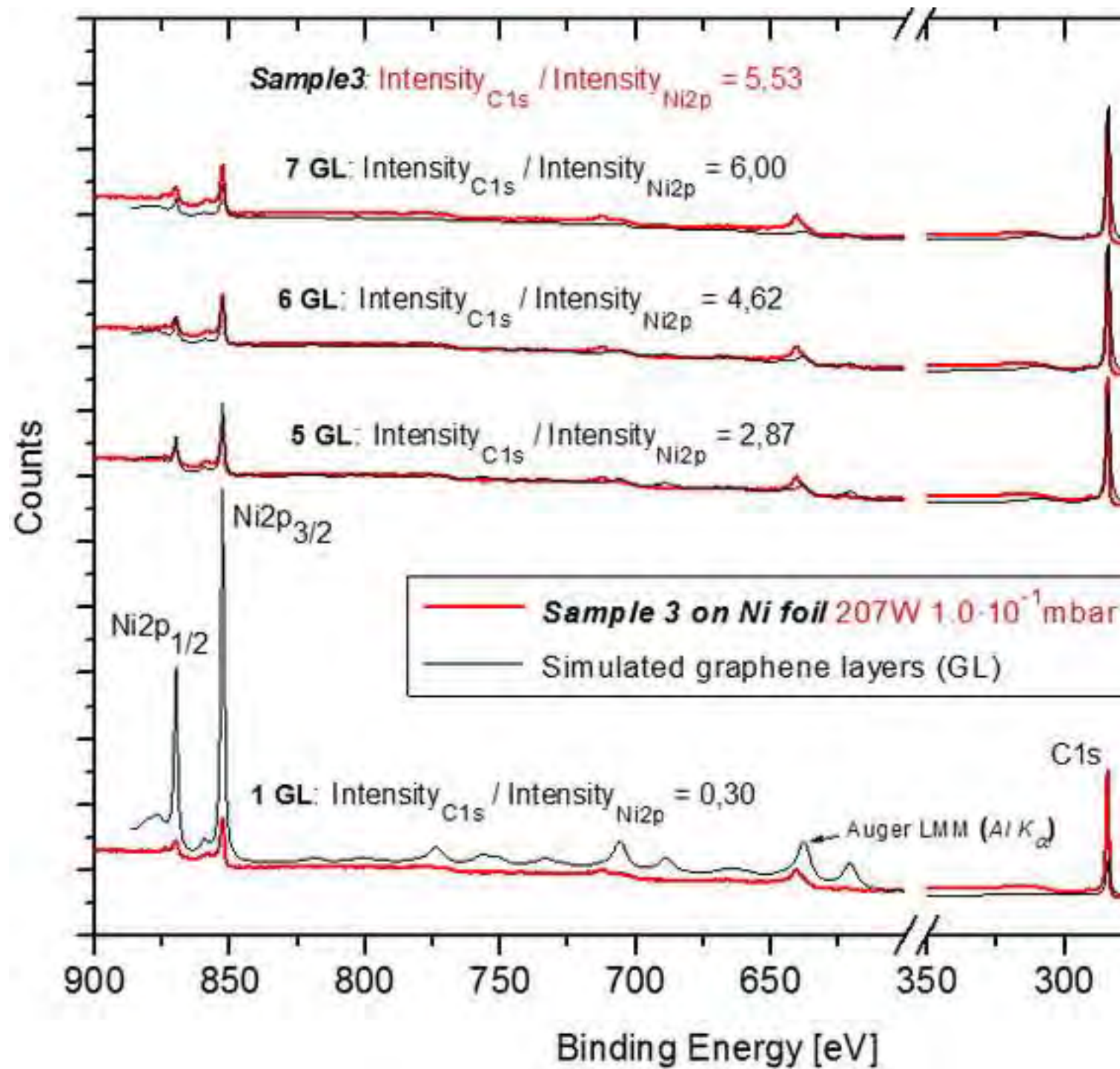
[Click here to download high resolution image](#)

Fig. 10a
[Click here to download high resolution image](#)

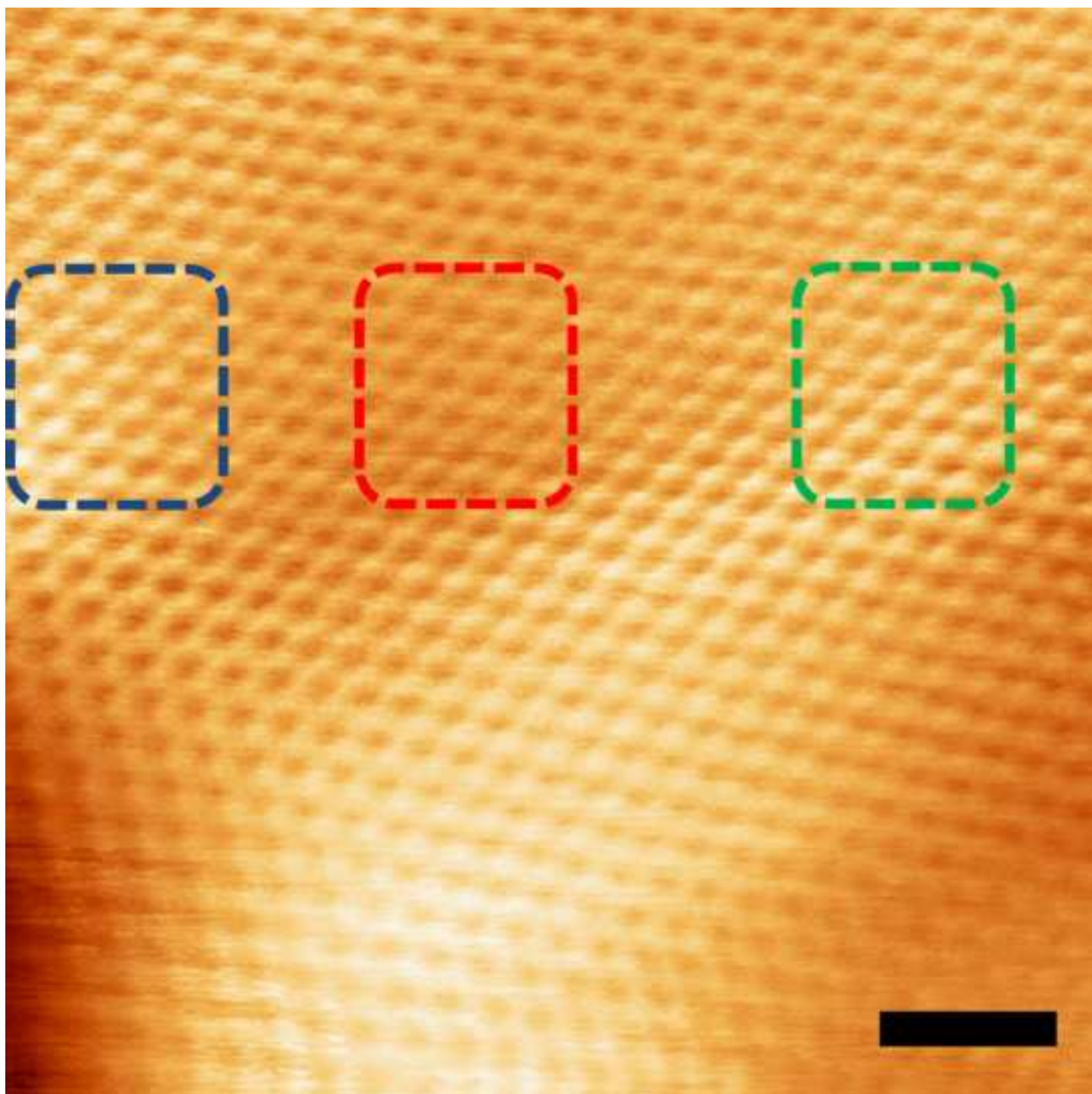


Fig. 10b

[Click here to download high resolution image](#)

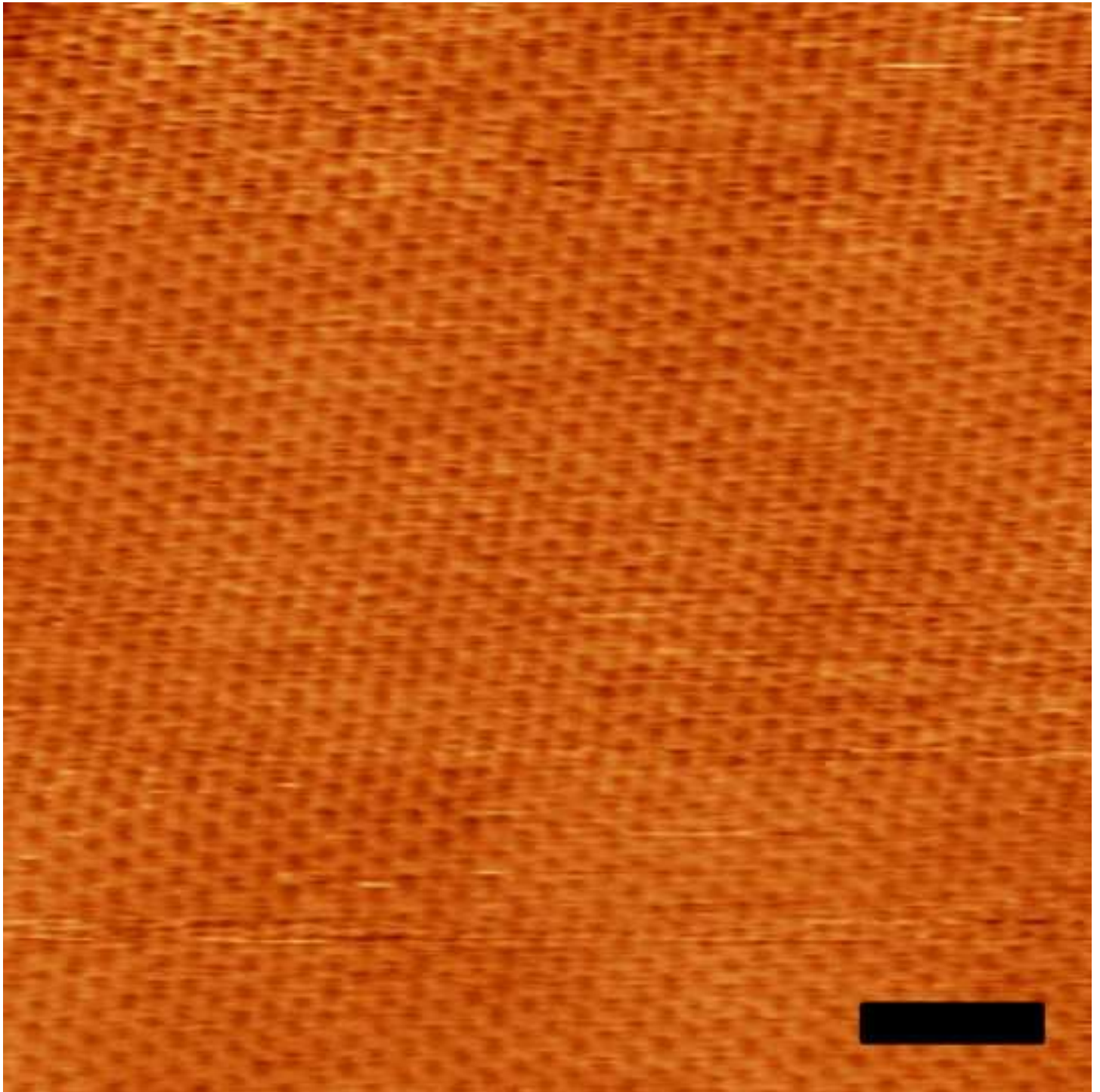


Fig. 10c
[Click here to download high resolution image](#)

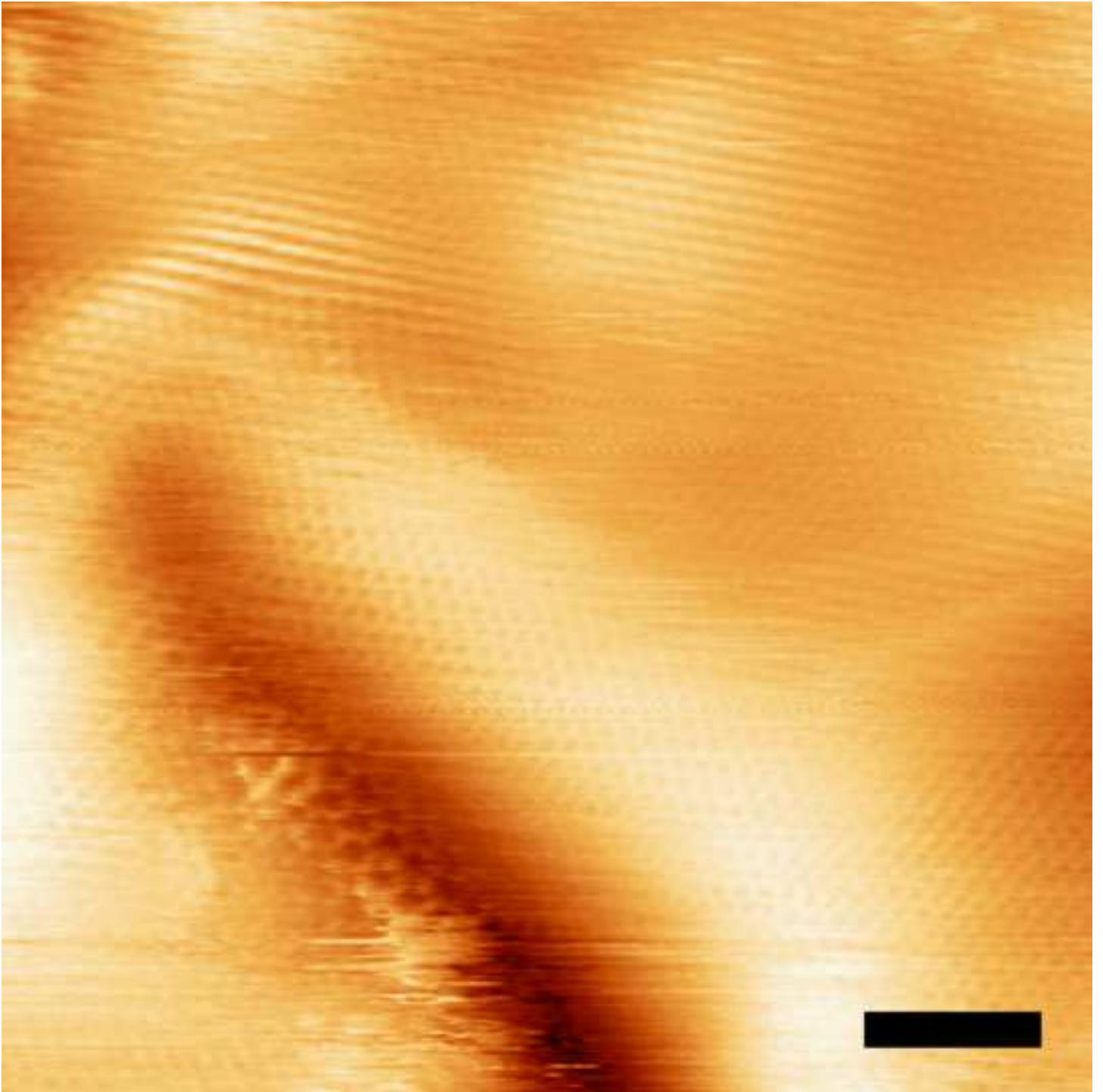


Fig. 11

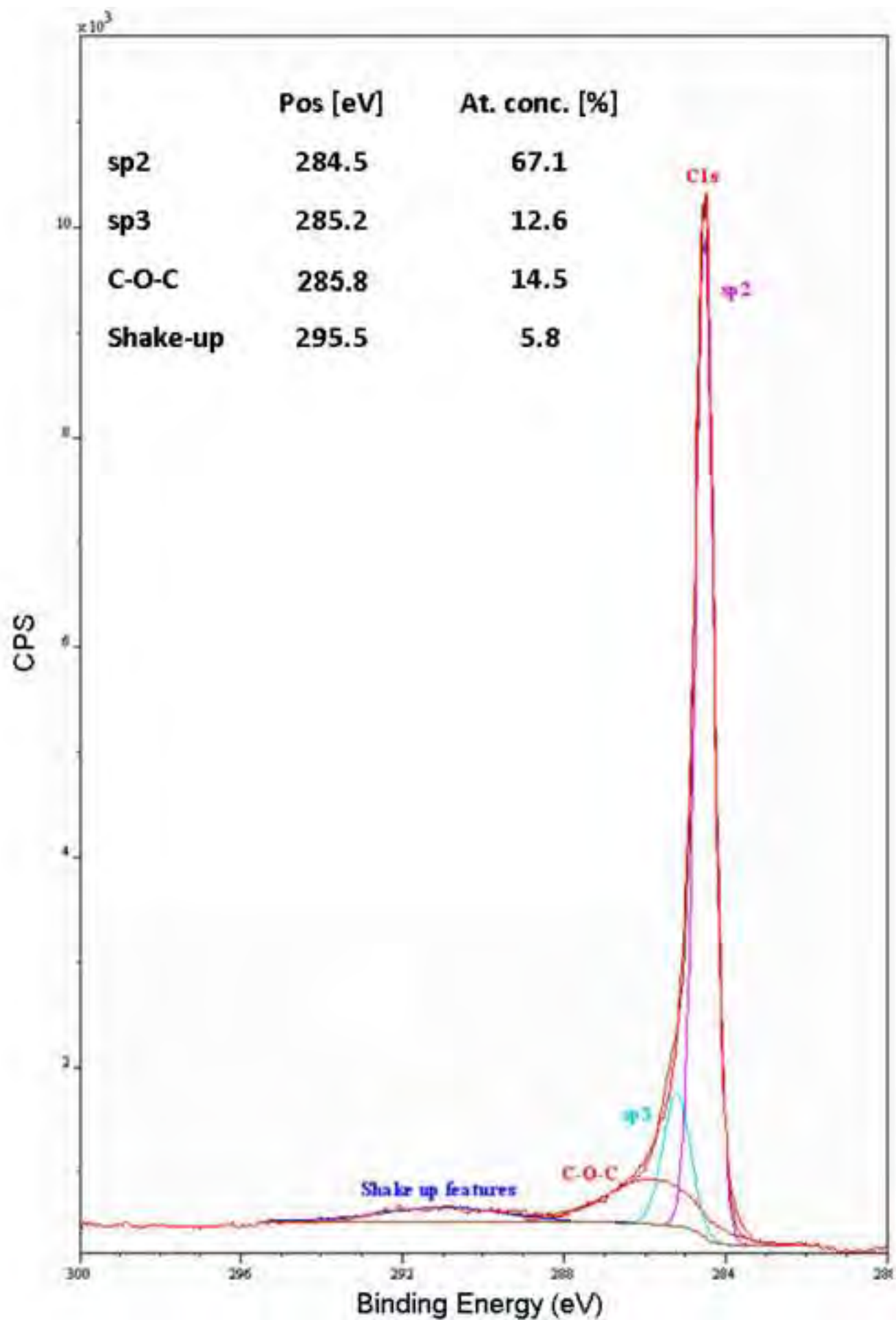
[Click here to download high resolution image](#)

Fig. 12

[Click here to download high resolution image](#)

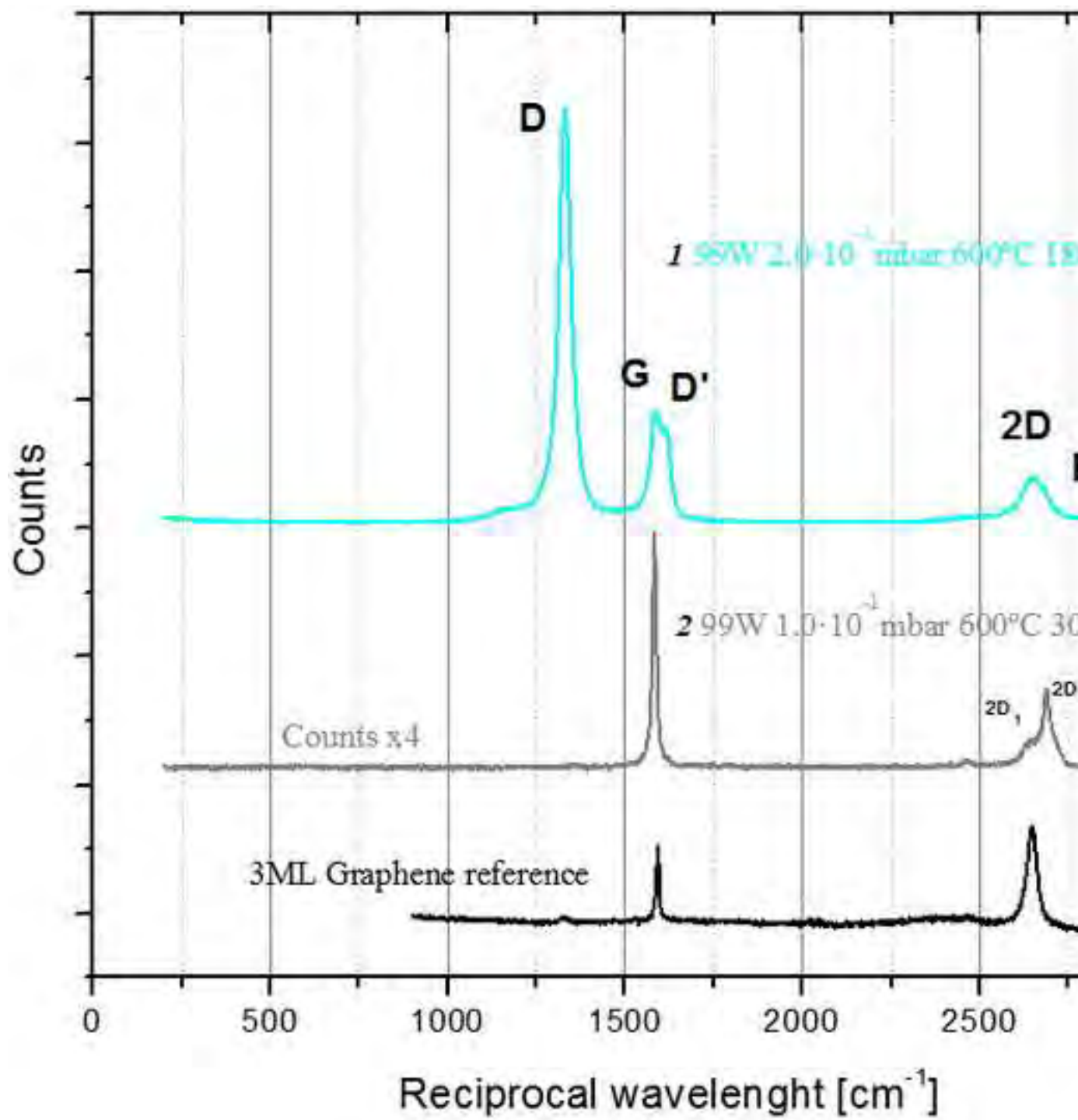


Fig. 13a

[Click here to download high resolution image](#)

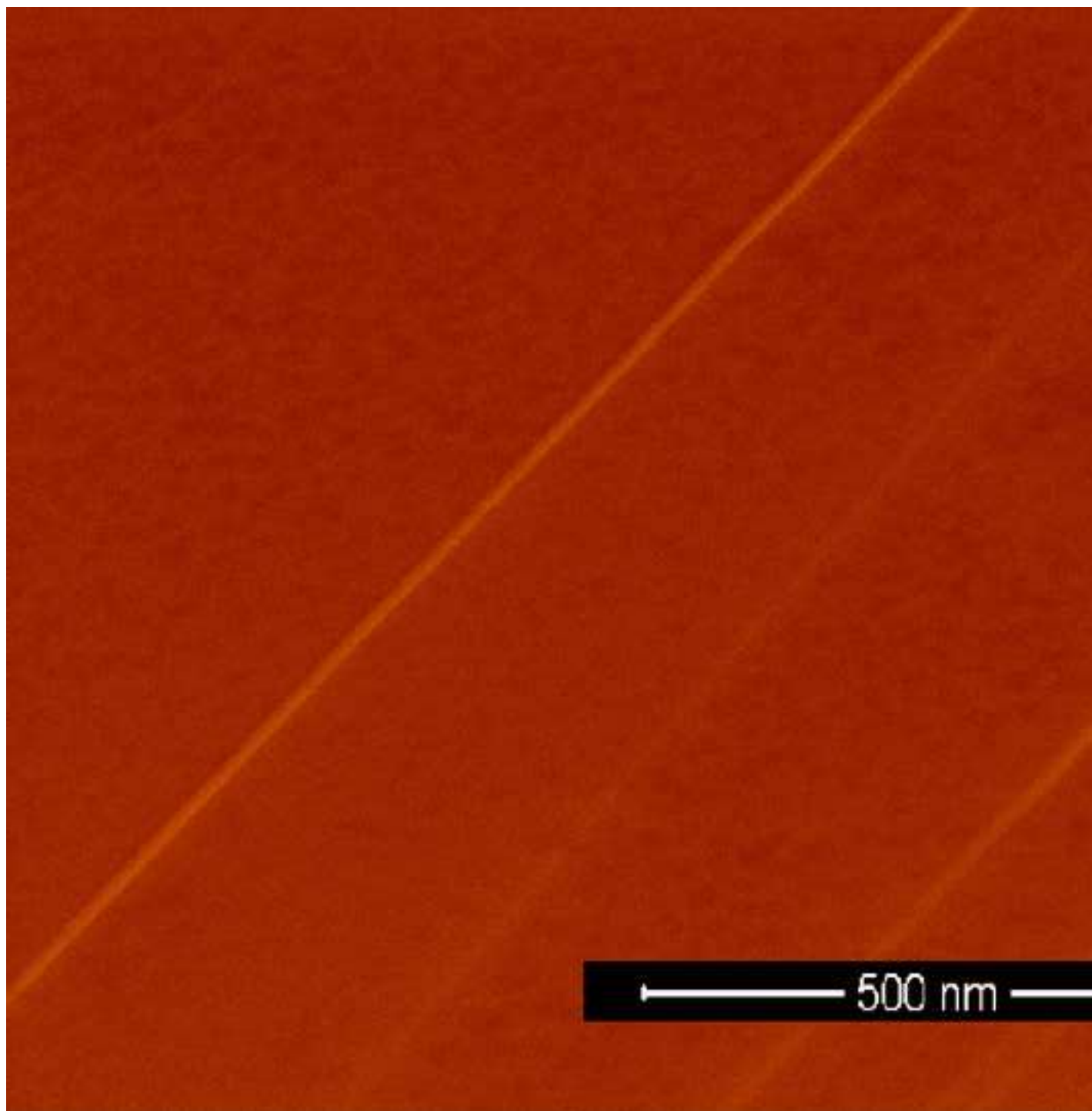


Fig. 13b

[Click here to download high resolution image](#)

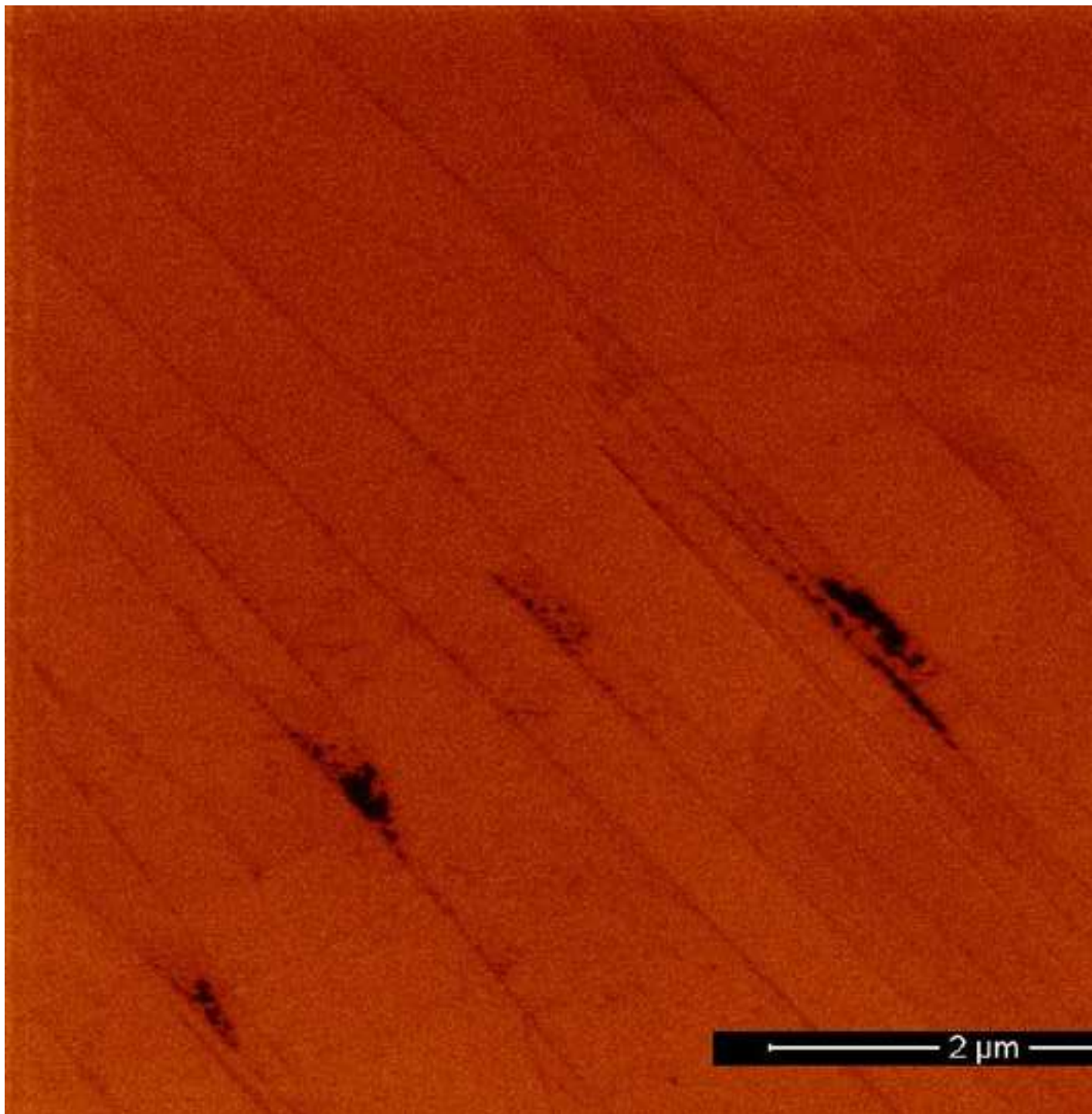


Fig. 13c

[Click here to download high resolution image](#)

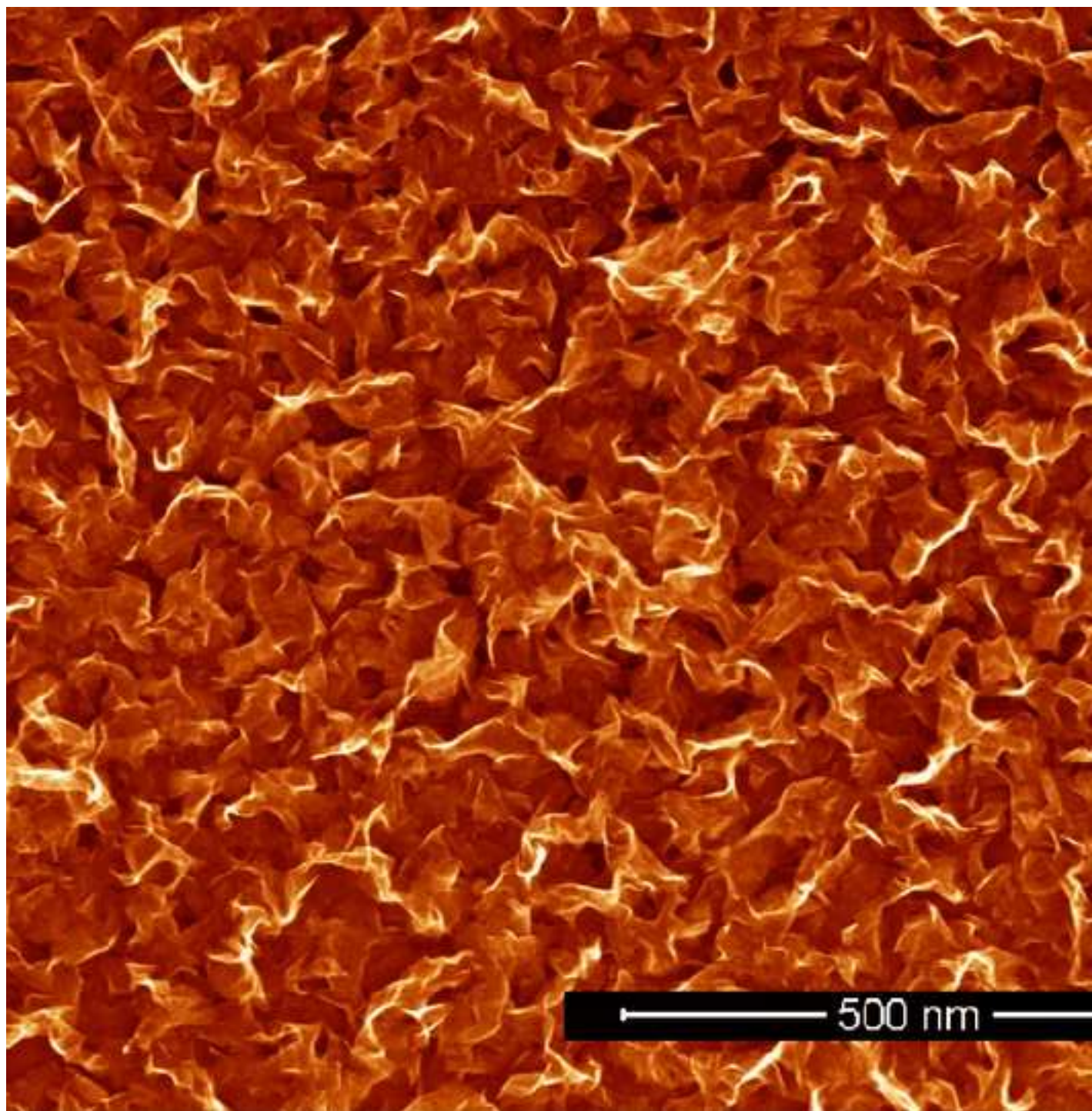


Fig. 13d

[Click here to download high resolution image](#)

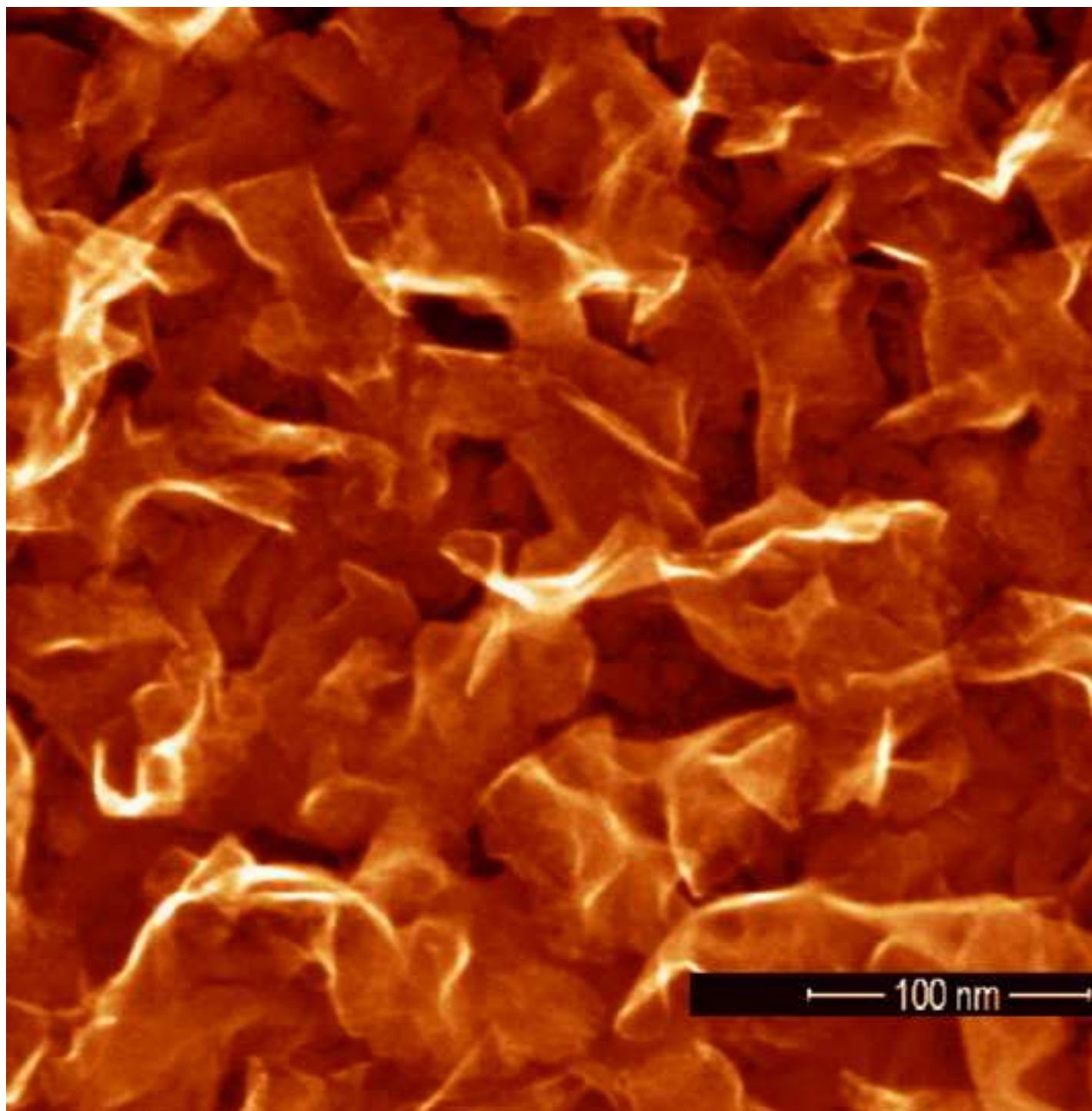


Fig. 14

[Click here to download high resolution image](#)